Monthly Notices of the ROYAL ASTRONOMICAL SOCIETY

MNRAS **525,** 1568–1587 (2023) https://doi.org/10.1093/mnras/stad2270
Advance Access publication 2023 July 26

Delayed appearance and evolution of coronal lines in the TDE AT2019qiz

P. Short [1]★ A. Lawrence [1]★ M. Nicholl [2] M. Ward,[3] T. M. Reynolds [4] S. Mattila,[5,6] C. Yin,[1] I. Arcavi,[7,8] A. Carnall [1] P. Charalampopoulos,[9] M. Gromadzki [10] P. G. Jonker,[11,12] S. Kim,[13,14] G. Leloudas,[9] I. Mandel [15,16] F. Onori [17] M. Pursiainen [9] S. Schulze [18] C. Villforth[19] and T. Wevers [20]

[1]*Institute for Astronomy, University of Edinburgh, Royal Observatory, Blackford Hill, Edinburgh EH9 3HJ, UK*
[2]*Birmingham Institute for Gravitational Wave Astronomy and School of Physics and Astronomy, University of Birmingham, Birmingham B15 2TT, UK*
[3]*Centre for Extragalactic Astronomy, Department of Physics, University of Durham, South Road, Durham, DH1 3LE, UK*
[4]*Cosmic Dawn Center (DAWN), Niels Bohr Institute, University of Copenhagen, 2200, Denmark*
[5]*Tuorla Observatory, Department of Physics and Astronomy, University of Turku, FI-20014 Turku, Finland*
[6]*School of Sciences, European University Cyprus, Diogenes Street, Engomi, 1516 Nicosia, Cyprus*
[7]*The School of Physics and Astronomy, Tel Aviv University, Tel Aviv 69978, Israel*
[8]*CIFAR Azrieli Global Scholars program, CIFAR, Toronto, ON M5G 1M1, Canada*
[9]*DTU Space, National Space Institute, Technical University of Denmark, Elektrovej 327, 2800, Kgs. Lyngby, Denmark*
[10]*Astronomical Observatory, University of Warsaw, Al. Ujazdowskie 4, PL-00-478 Warszawa, Poland*
[11]*SRON, Netherlands Institute for Space Research, Niels Bohrweg 4, NL-2333 CA, Leiden, the Netherlands*
[12]*Department of Astrophysics/IMAPP, Radboud University Nijmegen, P.O. Box 9010, NL-6500 GL, Nijmegen, the Netherlands*
[13]*Astro-engineering center (AIUC), Instituto de Astrofísica, Pontificia Universidad Católica de Chile, 7820436, Chile*
[14]*Max-Planck-Institut für Astronomie, Königstuhl 17, D-69117 Heidelberg, Germany*
[15]*Monash Centre for Astrophysics, School of Physics and Astronomy, Monash University, Clayton, Victoria 3800, Australia*
[16]*ARC Center of Excellence for Gravitational Wave Discovery – OzGrav, PO Box 218, Hawthorn VIC 3122, Australia*
[17]*INAF – Osservatorio Astronomico d'Abruzzo, via M. Maggini snc, I-64100 Teramo, Italy*
[18]*The Oskar Klein Centre, Department of Physics, Stockholm University, AlbaNova, SE-106 91 Stockholm, Sweden*
[19]*University of Bath, Department of Physics, Claverton Down, Bath BA2 7AY, UK*
[20]*European Southern Observatory, Alonso de Córdova 3107, Casilla 19, Santiago, Chile*

Accepted 2023 July 18. Received 2023 June 27; in original form 2022 July 8

ABSTRACT

Tidal disruption events (TDEs) occur when a star gets torn apart by a supermassive black hole as it crosses its tidal radius. We present late-time optical and X-ray observations of the nuclear transient AT2019qiz, which showed the typical signs of an optical-UV transient class commonly believed to be TDEs. Optical spectra were obtained 428, 481, and 828 rest-frame days after optical light-curve peak, and a UV/X-ray observation coincided with the later spectrum. The optical spectra show strong coronal emission lines, including [Fe VII], [Fe X], [Fe XI], and [Fe XIV]. The Fe lines rise and then fall, except [Fe XIV] that appears late and rises. We observe increasing flux of narrow H α and H β and a decrease in broad H α flux. The coronal lines have full width at half-maximum ranging from $\sim$150−300 km s^{-1}, suggesting they originate from a region between the broad- and narrow-line emitting gas. Between the optical flare and late-time observation, the X-ray spectrum softens dramatically. The 0.3–1 keV X-ray flux increases by a factor of $\sim$50, while the hard X-ray flux decreases by a factor of $\sim$6. *Wide-field Infrared Survey Explorer* fluxes also rose over the same period, indicating the presence of an infrared echo. With AT2017gge, AT2019qiz is one of two examples of a spectroscopically confirmed optical-UV TDE showing delayed coronal line emission, supporting speculations that Extreme Coronal Line Emitters in quiescent galaxies can be echos of unobserved past TDEs. We argue that the coronal lines, narrow lines, and infrared emission arise from the illumination of pre-existing material likely related to either a previous TDE or active galactic nucleus activity.

Key words: accretion, accretion discs – black hole physics – transients: tidal disruption events.

1 INTRODUCTION

A tidal disruption event (TDE) occurs when a star's orbit brings it within the tidal radius of its host galaxy's central supermassive black hole (SMBH). The star is subsequently ripped apart, releasing a luminous flare as the stellar material falls back on to the SMBH (Hills 1975; Rees 1988). Early TDE candidates were discovered via soft X-ray flares (e.g. Komossa & Bade 1999; Komossa & Greiner 1999), with luminosities of $\sim$10^{44} erg s^{-1} and light curves matching the $t^{-5/3}$ decay rate expected from theory (Hills 1975; Rees 1988). Since then, a variety of nuclear transients and extreme

★ E-mail: shortphilip4@gmail.com (PS); al@roe.ac.uk (AL)

variables has been observed, but a consistent class of optical-UV transients has emerged which are widely accepted as being TDEs (van Velzen et al. 2020; Gezari 2021). The key features that define this class include (i) a large amplitude nuclear optical flare; (ii) a rise time of ∼days-weeks and a decay time of ∼weeks-months; (iii) extremely broad and weak emission lines from hydrogen and helium; (iv) a blue continuum with effective temperature around 10–30 000 K; and (v) roughly constant optical colours during the decay. We refer to members of this class as 'spectroscopically confirmed optical-UV TDEs.' Strictly, speaking it is not rigorously proved that these events result from the disruption of a star, but most workers accept that a TDE is the most likely explanation, and so refer to these objects simply as 'TDEs' rather than for example 'candidate TDEs'. Empirically, they form a well-defined class which is distinct from either known types of supernovae (SNe), or extreme active galactic nucleus (AGN) variables such as Changing Look AGN.

Even within this consistent class, there is a detailed diversity. The appearance or lack of hydrogen, helium, and Bowen fluorescence emission lines divides these optically selected TDEs into three classes; TDE-H, TDE-He, and TDE-H + He (Arcavi et al. 2014; Leloudas et al. 2019; van Velzen et al. 2021b). It has been shown that the strengths of these lines can vary as the TDE evolves (e.g. Nicholl et al. 2019; Charalampopoulos et al. 2022; Onori et al. 2022), allowing TDEs to transition between classes. In addition, other features have been observed such as Fe II lines (Wevers et al. 2019b; Cannizzaro et al. 2021) and double-peaked emission lines (Hung et al. 2020; Short et al. 2020; Wevers et al. 2022). TDEs are also extremely diverse in their X-ray to optical ratios, ranging from $\sim 10^{-4}$ to 1 (Auchettl, Guillochon & Ramirez-Ruiz 2017). This could indicate that some TDEs form accretion disks quickly while others do not, or that X-rays are heavily absorbed/re-processed by an atmosphere or outflow along the observer's line of sight (e.g. Loeb & Ulmer 1997; Guillochon, Manukian & Ramirez-Ruiz 2014; Roth et al. 2016; Dai et al. 2018; Roth & Kasen 2018).

Given that optical-UV TDEs are seen to occur in systems with black hole masses $10^{6-7} M_\odot$ (Wevers et al. 2017; Nicholl et al. 2022), one would expect a compact accretion disc to have a temperature $T \sim 10^6$ K, at odds with the observed temperatures of $T \sim 2{-}4 \times 10^4$ K. This may be explained by reprocessing (see paragraph above), but is the expected EUV continuum actually there? One test is to look for emission from highly ionized species.

Prior to the current era of optical sky surveys, Komossa et al. (2008) discovered fading high-ionization coronal iron emission lines, He II and double-peaked Balmer lines in the nearby galaxy Sloan Digital Sky Survey (SDSS, Adelman-McCarthy et al. 2008) J095209.56+214313.3 (J0952+2143) during a search for emission-line galaxies in SDSS Data Release 6 (DR6). Optical photometry showed a peak in optical brightness in 2004, with an increase towards the NIR which was inconsistent with previous 2MASS observations. *GALEX* (Martin et al. 2005) data also showed a rise in UV flux. Wang et al. (2011) found a similar example of coronal line emission in the galaxy SDSS J074820.67+471214.3 which also had an optical flair, and went on to find 5 more in a systematic search for such objects (Wang et al. 2012). These authors proposed that the most likely cause of such coronal emission was an earlier, unobserved, TDE in a gas rich environment. Of the five new events reported by Wang et al. (2012), three had fading iron lines as found by Yang et al. (2013), making these and J0952+2143 the strongest candidates for ECLEs that are caused by illumination by an earlier TDE. The case for J0952+2143 was made stronger, when a clear infrared echo was found Komossa et al. (2009), and when the associated optical flare was covered more densely in LINEAR data (Palaversa et al. 2016) retrospectively.

In this scenario, the broad low-ionization emission lines come from re-processing of UV/X-ray flares by outflows directly connected with the TDE in question, which matches well the line profiles of H α and He II (Roth & Kasen 2018), while the coronal lines originate from interactions with a clumpy interstellar medium or other pre-existing material. If produced by photoionization, the coronal lines imply an ionizing continuum extending into the X-rays, requiring ionizing potentials of up to nearly 400 eV in the case of [Fe XIV]. Coronal lines are not uncommon in AGN (Grandi 1978; Penston et al. 1984; Gelbord, Mullaney & Ward 2009), where we also expect a hard ionizing continuum.

It is therefore important to test for the presence of highly ionized species in the class of well-confirmed optical-UV TDEs, where we have high-quality optical, X-ray, and spectroscopic data at the time of the actual flare. Coronal lines have so far only been observed in one such clear optical-UV TDE to date, AT2017gge (Onori et al. 2022). The lines appeared in this event from ∼200 to 1700 d after the optical light curve peak. Another potential candidate for a TDE showing coronal lines is the nuclear transient AT 2019avd. Malyali et al. (2021) observed [Fe X] and [Fe XI] emission lines accompanied by a rise in X-ray flux, and Chen, Dou & Shen (2022) argue that this event could be interpreted as a TDE. However, observationally it is definitely not a member of our well defined class of optical-UV TDEs – it has a double peaked light curve, and relatively strong and narrow Balmer lines. There was also a tentative detection of coronal lines in the nuclear transient PS16dtm (Petrushevska et al. 2023). Like AT 2019avd, it does not show all the classic signs of the optical-UV TDE class, but is nonetheless argued to be a TDE by Petrushevska et al. (2023).

As well as exhibiting coronal lines, AT2017gge was also exceptionally luminous in the infrared (IR). This IR emission arises from an IR echo, in which dust in the vicinity of the SMBH absorbs UV/optical emission produced by the TDE, and re-radiates this energy in the IR. IR echoes have previously been observed in approximately half of optically discovered TDEs, but typically the total proportion of luminosity arising from the dust is small, implying that the covering factor is only ∼1 per cent of that observed in the UV/optical (Jiang et al. 2021). The covering factor derived for the IR echo associated with AT2017gge was ∼20 per cent (Wang et al. 2022), much larger than typical TDEs discovered in optical and occurring in quiescent galaxies, and indicating the presence of a larger quantity of dust. AT2019avd also exhibited an abnormally bright IR echo (Malyali et al. 2021; Chen et al. 2022), further suggesting a connection between these phenomena.

The subject of this work is AT 2019qiz, a clear member of the optical-UV TDE class first identified on 2019-09-19 (Forster 2019) at a redshift of $z = 0.0153$, and reaching a peak at 2019-10-10. *Gaia* data (Gaia Science Alerts Hodgkin et al. 2013) show no further activity in the optical light curve since the decline from this peak. The transient was analysed in detail by Nicholl et al. (2020) and Hung et al. (2021). Light-curve fitting results suggested that the flare was produced by a $\sim 1\,M_\odot$ star being disrupted by a $\sim 10^6\,M_\odot$ black hole. The black hole mass derived from the TDE light curve was consistent with that derived from velocity dispersion measurements and $M{-}\sigma$ relations. Early optical spectra show broad, asymmetric H and He II lines, which Nicholl et al. (2020) argued were driven by an expanding outflow. The lines became more symmetrical as the TDE evolved. He II was replaced by N III λ4641 via Bowen fluorescence (Nicholl et al. 2020; Hung et al. 2021), which occurs when recombining He II produces an EUV photon which

goes on to excite some O III and N III states. These subsequently recombine producing 'Bowen fluorescence' lines. UV spectra show high-ionisation broad absorption lines (HiBALs) and Fe and low-ionization broad absorption lines (FeLoBALs; Hung et al. 2021). Unfortunately, there are no spectra of the host galaxy (2MASX J04463790-1013349) taken before the flare. Both studies suggest that the host galaxy harbours a weak AGN based on Baldwin–Phillips–Terlevich (BPT) diagrams. Early X-ray detections suggest accretion started promptly in this event (Nicholl et al. 2020), though the high hardness ratio may indicate that the X-ray emission originates from the pre-existing AGN (Hung et al. 2021). However, Nicholl et al. (2020) note that the hardness ratio varied during outburst, implying that the TDE did affect the X-ray emission.

In this paper, we present and analyse two new spectra of AT2019qiz obtained with X-Shooter taken 428 and 828 rest-frame days after the optical light-curve peak, a MUSE spectrum obtained 481 rest-frame days after optical peak and *Swift* XRT data taken 816 rest-frame days post optical peak, as well as re-examining the spectra taken during the campaign of Nicholl et al. (2020). In Section 2, we detail our observations and data reduction process. In Section 3, we present our spectroscopic analysis, in Section 4 we present analysis of *Swift* UV and X-ray data, and in Section 5 we construct an SED of the TDE in outburst. In Section 6, we present analysis of NEOWISE IR data. In Section 7, we discuss and interpret our results and analysis, and in Section 8, we provide a summary and conclusion to this work.

2 OBSERVATIONS AND DATA REDUCTION

2.1 X-Shooter

Observations were made on 2020-12-15 and 2022-01-26 with the X-Shooter instrument (Vernet et al. 2011) mounted on UT3 at the Very Large Telescope (VLT) in ESO's Paranal observatory, Chile. X-Shooter is an intermediate resolving power spectrograph with a wavelength range spanning 3000–25 000 Å. The spectrograph consists of three arms; the UVB arm which covers 3000–5595 Å, the VIS arm which spans 5595–10 240 Å and the NIR arm that ranges from 10 240 to 24 800 Å. Slit widths of 1.0, 0.9, and 0.9 arcsec were used for the UVB, VIS and NIR arms, respectively, giving respective resolving powers of $R = 5400$, 8900, and 5600. Data were obtained under programs 106.21SS.001 (PI Short) and 108.22J7.001 (PI Nicholl). We refer to these spectra throughout this paper as the 2020 December and 2022 January spectra, respectively.

Data reduction was performed using the X-Shooter pipeline recipes and the EsoReflex GUI environment (Freudling et al. 2013). The NIR arm was reduced in NOD mode, while the UVB and VIS arms were reduced in STARE mode that was found to improve the signal to noise. Telluric corrections were performed in the VIS arm using telluric standards observed before and after the observations at a similar position to the target. Telluric features in the NIR arm proved difficult to correct and, as this wavelength region contained no features of interest, this arm was not used in the rest of our analysis. Extinction correction was performed using the Fitzpatrick (1999) model in the EXTINCTION[1] package in PYTHON, with reddening values from the NASA/IPAC Infrared Science Archive (Schlafly & Finkbeiner 2011). As the optical continuum luminosity at this phase is dominated by the host galaxy, the spectra were flux corrected using the PYSYNPHOT PYTHON package (STScI Development Team 2013) to an aperture-matched host *r*-band mag of 16.47 as determined in Nicholl et al. (2020). The reduced spectra are displayed in Fig. 1.

[1]https://extinction.readthedocs.io/en/latest/

2.2 MUSE

We observed the field on 2021-02-08 with the panoramic integral-field spectrograph MUSE (Bacon et al. 2010), mounted at UT4 at ESO's VLT, in the seeing-enhanced adaptive optics wide-field mode (WFM-AO) under clear condition and DIMM seeing <0.6 arcsec. MUSE WFM-AO has a large field of view covering 1 arcmin × 1 arcmin and a high spatial sampling of 0.2 arcsec × 0.2 arcsec. It covers the wavelength range from 4650 to 9300 Å with a spectral resolving power of 2000–4000. The observation consists of three 1100-s exposures that were dithered by 1–2 arcsec and rotated by 90° with respect to each other. We retrieved the reduced science-ready datacube from the ESO archive, which was reduced with the ESO MUSE pipeline version 2.8.4 (Weilbacher et al. 2020). We extracted the spectrum of the host galaxy nucleus using a circular aperture with a diameter of 1 × FWHM (stellar PSF). The integral field of MUSE also allows us to check for spatial extent. The host starlight is of course very extended, but the emission line source is compact. Comparing extractions with 1 arcsec and 2 arcsec apertures changed the [O III] flux by ∼15 per cent. Given the other uncertainties, this gives us reasonable confidence in both the Xshooter and MUSE line flux values.

2.3 Neil Gehrels *Swift* observatory

A *Swift* (Gehrels et al. 2004) observation was made on 2022-01-13 using the XRT instrument in photon-counting mode and the UVOT instrument with the UVW2 filter (Obs ID: 00012012043, PI Short). The XRT data were reduced and a spectrum was generated using the online *Swift* XRT product builder (Evans et al. 2009). The UVOT UVW2 flux was measured using a 5 arcsec aperture, approximately twice the UVOT point-spread function. This matches the aperture used to extract earlier UVOT photometry by Nicholl et al. (2020). The count rates were obtained using the *Swift* UVOTSOURCE tools and converted to magnitudes using the UVOT photometric zero points (Breeveld et al. 2011). The analysis pipeline used software HEADAS 6.24 and UVOT calibration 20170922. We note that the calibration files have since been updated, but we use the older calibration for consistency with Nicholl et al. (2020). We measured UVW2 AB magnitude of 20.58 ± 0.04 which is consistent with the host magnitude measured in (Nicholl et al. 2020) of 20.51 ± 0.2, suggesting there is no detectable contribution from the TDE.

2.4 NEOWISE survey

We obtained MIR data of AT 2019qiz taken as part of the NEOWISE survey (Mainzer et al. 2011, 2014) from the public NEOWISE-R Single Exposure (L1b) Source Table.[2] NEOWISE observes the entire sky at 6 month intervals, with multiple observations at each 'visit'. We adopted the median value of the individual measurements at each visit as the magnitude, removing measurements flagged as poor quality or separated from the coordinates of AT 2019qiz by more than 2 arcsec. For the uncertainty, we adopted the standard error of mean of the individual measurements taken at each bi-yearly epoch of WISE observation after 3σ-clipping outliers. We added 0.0026 and 0.0061 mag uncertainties in quadrature to the *W*1 and *W*2 measurements, respectively, which are the RMS residuals found in the photometric calibration during the survey period. No extinction correction was made to the *WISE* magnitudes.

[2]https://irsa.ipac.caltech.edu/cgi-bin/Gator/nph-scan?mission=irsa&submit=Select&projshort = WISE

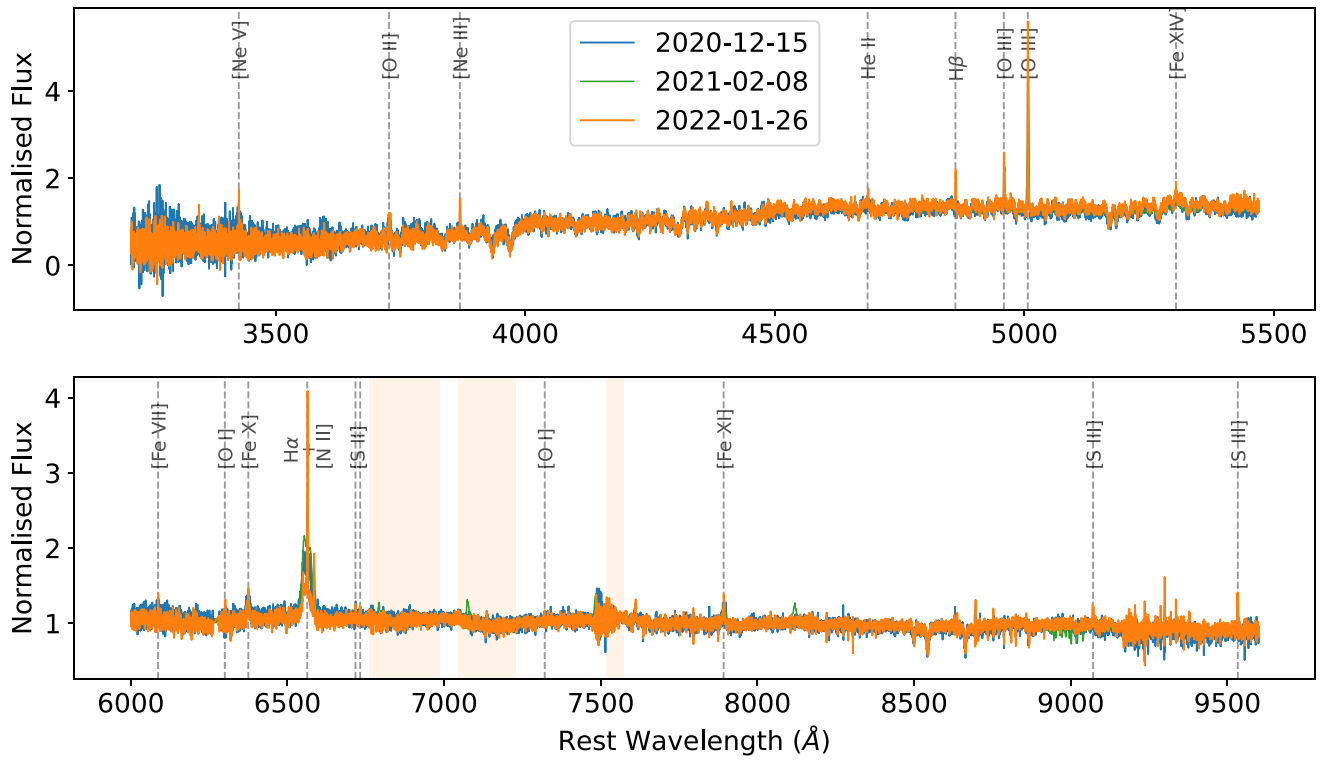

Figure 1. The reduced X-Shooter and MUSE spectra. The X-Shooter spectra are binned for ease of viewing. Emission line identifications are marked with the grey dashed lines. The upper plot covers the X-Shooter UVB arm wavelength range, while the lower plot covers the VIS arm. The 'emission' features redwards of ∼6800 Å in the MUSE (green) spectrum are residuals from telluric corrections. The fluxes are scaled to approximately match the stellar continuum in each case.

3 SPECTROSCOPIC ANALYSIS

3.1 Host black hole mass

Nicholl et al. (2020) follow the method of Wevers et al. (2017, 2019a) to fit the velocity dispersion of stellar absorption lines using PPXF (Cappellari 2017). They used an X-Shooter spectrum obtained 140 d after optical light-curve peak, and measured a velocity dispersion of 70 ± 2 km s^{-1}. We use the same method on our X-Shooter spectra and measure a value of 72 ± 1 km s^{-1}, consistent with that measured in Nicholl et al. (2020). Using the relations of McConnell & Ma (2013), Gültekin et al. (2009) and Kormendy & Ho (2013) our velocity dispersion measurement yields black hole masses of $\log_{10}(M_{\rm BH}/{\rm M}_\odot) = 5.82 \pm 0.41$, 6.24 ± 0.48, and 6.54 ± 0.32, respectively. Both Nicholl et al. (2020) and Hung et al. (2021) obtain additional black hole mass estimates from UV and optical light-curve model fits, deriving values of $\log_{10}(M_{\rm BH}/{\rm M}_\odot) = 5.89^{+0.05}_{-0.06}$ and 6.14 ± 0.10, respectively. These are both consistent with the estimate from the velocity dispersion. Additionally, Nicholl et al. (2022) re-fit the light curve after correcting for a calibration error affecting UVOT photometry at the time of the AT2019qiz outburst. The slightly increased value of $\log_{10}(M_{\rm BH}/{\rm M}_\odot) = 6.22$ is still consistent with the velocity dispersion results. Given the range of estimated values, for simplicity we assume an intermediate SMBH mass of $M_{\rm BH} = 10^6$ M$_\odot$ for the remainder of this analysis, but note that this has an uncertainty of at least a factor of 2.

3.2 Low ionization lines

The spectra feature narrow emission lines, including [O II], [O III], [N II], [S II], H α, and H β, as well as broad H α. The H β and H α regions are displayed in Fig. 2. To measure the flux and widths of each line we use the PYTHON package LMFIT[3] to fit a single Gaussian component to the line and a polynomial component to the local continuum in that line region. In order to separate the narrow H α and [N II] emission lines from the broad H α feature, we fit the entire region with 5 Gaussian components simultaneously. The broad feature is not well fit by a single Gaussian so we fit two components to this, while the remaining three components are fit to the narrow H α and [N II] $\lambda\lambda$ 6549, 6584 Å lines. The [N II] λ6584 Å/λ6549 Å ratio is fixed to 3 and the [N II] λ6549 Å line width is fixed to match that of the 6584 Å line. The fits, shown in the right-hand panel of Fig. 3, were performed on both X-Shooter spectra and the MUSE spectrum and provide a satisfactory fit, hinting that the broad line may be double peaked. When measuring H β, an absorption component is clearly visible which we fit separately. A stellar absorption feature is likely obscured in the H α blend, meaning that the total H α flux could be underestimated. Flux measurements of all emission lines are shown in Tables A1–A3. We note that the third spectrum seems to have an anomalous [O III] 5007/4959 ratio. However, the ratio of peak values is much closer to the expected value of 3. There is an additional systematic error in deriving line fluxes that arises from the uncertain line wings in the presence of both noise and structured stellar continuum. We estimate this systematic error to be ∼15 per cent of the line flux.

There are a number of changes in the emission lines from the 2020 December spectrum to the 2022 January spectrum. The broad H α line increases in flux from the 2020 December to 2021 February spectra but then drops again in the 2022 January spectrum.

[3] https://lmfit.github.io/lmfit-py/

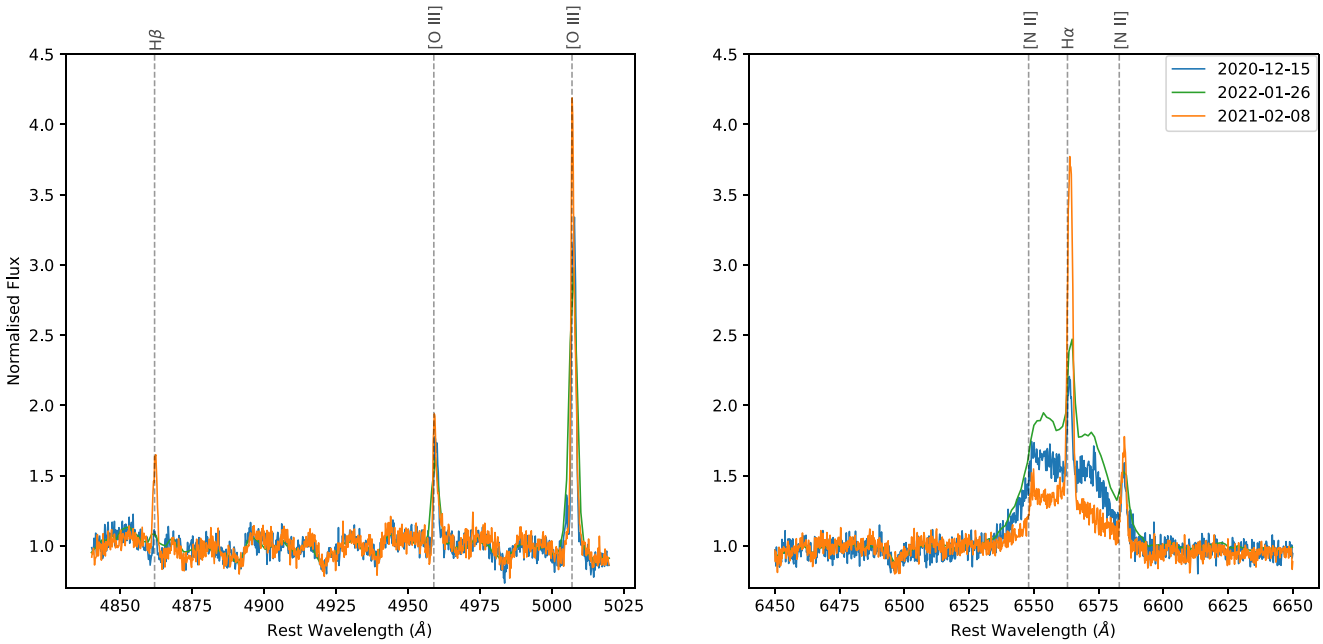

Figure 2. The H β + [O III] and H α regions for our late-time spectra. The narrow Balmer lines have brightened considerably over time, while the broad H α has risen in the 2021 February (green) spectrum before dimming again in the 2022 January spectrum (orange).

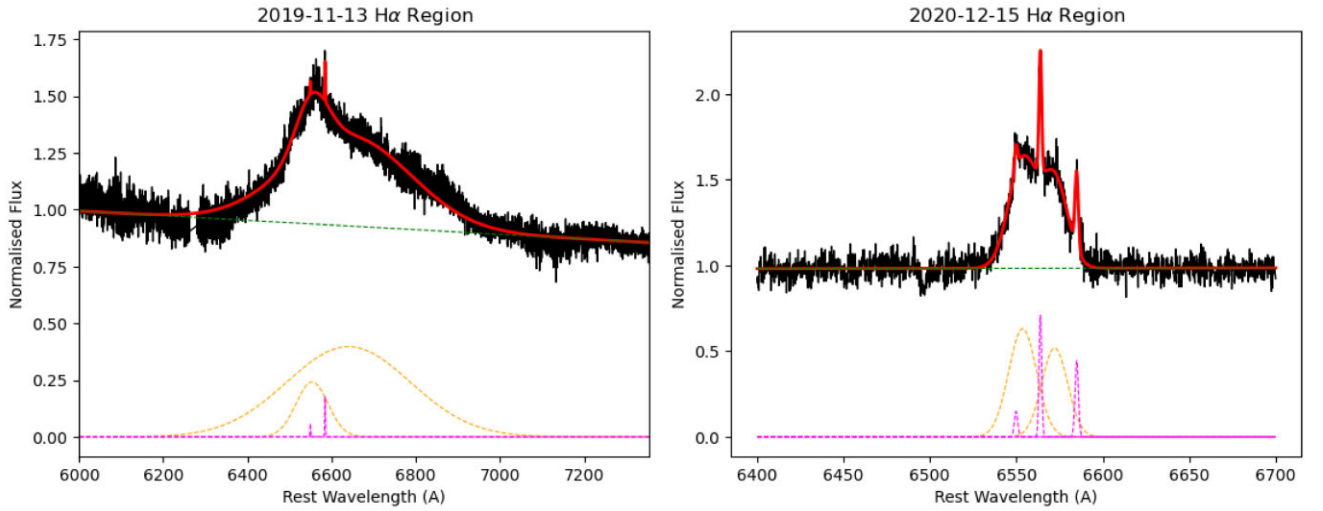

Figure 3. Fits to H α regions in (left) an early X-Shooter spectra obtained 20 191 113 and (right) our 2020 December spectrum. In both cases, the broad H α feature is well fit by two broad Gaussian components, though in the earlier spectra the second component is much broader and offset.

Meanwhile, the narrow H α, H β, and [S III] lines increase in strength. The [O III] lines do not change significantly. We also observe the appearance of [O I] λ6300 Å and He II λ4686 Å in the 2022 January spectrum, neither of which were detectable in the previous spectra.

In Fig. 4, we plot the evolution of both broad and narrow H α emission over time. We use X-Shooter spectra from Nicholl et al. (2020) dating back to ∼35 d after optical lightcurve peak to show the complete evolution. In the spectra from Nicholl et al. (2020), there are two broad components but one is consistently broader and redshifted. Nicholl et al. (2020) determine this is possibly due to an outflow so we exclude it from our measurements. An example fit to these earlier spectra is included in Fig. 3. The broad-line evolution initially follows a downward trend but increases again at some point between ∼130 and 481 d (our 2020 December spectrum). It peaks at 481 d (our 2021 February spectrum) before declining again. The narrow-line emission appears to be increasing. This is presumably due to photons from the initial outburst illuminating material at large radii. The fact that this is taking place gradually over an extended time, rather than a simple spike at a time delayed from the outburst, indicates that the material is spread over a large range of distances and/or angles. We note that an increase in narrow line flux was also observed in the other coronal line emitting TDE (AT2017gge; Onori et al. 2022). In addition, Wang et al. (2011, 2012) see [O III] increase after the coronal lines have faded in the Extreme Coronal Line Emitters which they proposed to be the echoes of TDEs.

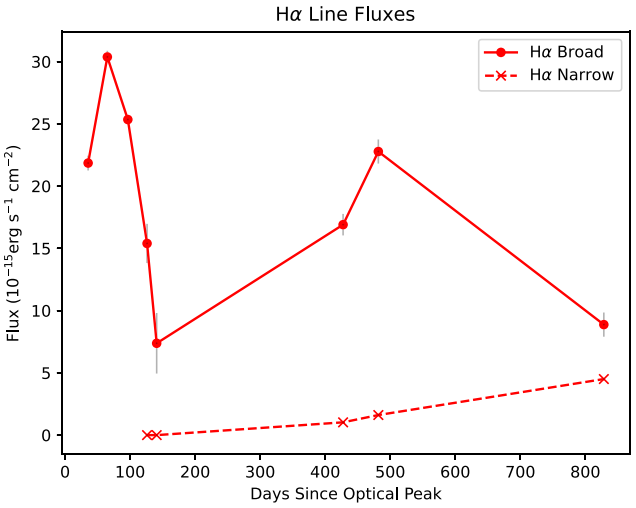

Figure 4. The evolution of both the broad and narrow H α emission line components using spectra from Nicholl et al. (2020) and the spectra presented in this paper. In the first three spectra, there is a second broad outflow component which we omit from our measurements. Errorbars are included but in some cases too small to be visible.

The fact that the Balmer line increase has not yet come to a clear maximum means that we do not yet have a clear picture of the radial and angular distribution of the related gas. However, we can ask whether what we see so far is consistent with the kinematic information. We have neither a kinematic or spatial model, but a reasonable expectation is that line widths will be of the order of the virial velocity at the corresponding distance, so that we can estimate distance crudely as $r = GM/v^2_{\rm FWHM}$, using a black hole mass of $M = 10^6$ M$_\odot$. Balmer line widths are $\sim$80 km s^{-1} indicating a distance of 2.2 light years. However at this distance, the gas may be responding to the galaxy potential as much as the black hole, so that this distance should be considered a lower limit. This is consistent with the fact that Balmer line response has not yet peaked; on the other hand, there clearly is significant material already responding at delays less than 2 yr, indicating that the illuminated material is distributed over a large range of radii and/or angles.

In order to determine the source of the narrow-line emission we plot our measurements on BPT diagrams (Baldwin, Phillips & Terlevich 1981; Veilleux & Osterbrock 1987; Kauffmann et al. 2003) in Fig. 5. We use the 2020 December and 2022 January X-Shooter measurements as well as the 2020-02-28 spectrum from (Nicholl et al. 2020). We do not use the 2021 February measurement as H β is not resolved in the MUSE spectrum. H β is difficult to measure in the 2020-02-28 spectrum that gives rise to a large errorbar; however, the [N II]/H α and [S II]/H α ratios clearly place the galaxy in the AGN region rather than star formation. In the 2020 December spectrum, the narrow lines look to clearly have an AGN origin, but in the 2022 January spectrum the emission looks more like a star-forming region. We would expect the ionizing continuum for a TDE to be similar to that for an AGN, but any changes in the ionizing continuum could cause the line ratios to change. Detailed modelling of TDE emission lines is planned for future work.

Using the 2022 January spectrum, we calculate an He II/H β ratio of 0.33 ± 0.05. Assuming both lines are produced via photoionization, this reflects the relative intensity of the ionizing continuum at 912 Å and 228 Å. If the continuum in this region is a power law then we can calculate the index α using $I_{4686}/I_{4862} \propto (912/228)^\alpha$ (Penston & Fosbury 1978). With our measured ratio we calculate $\alpha = -1.3 \pm 0.1$. We use this to help construct the SED in Section 5.

3.3 Coronal lines

The most interesting features in our spectra are the highly ionized iron lines [Fe VII] λ6087, [Fe X] λ6375, [Fe XI] λ7892, and [Fe XIV] λ5304, as well as [Ne V] λ3426. In Fig. 6, we display [Fe] line regions from all three of our recent spectra. The most notable change is the appearance of [Fe XIV] in the 2021 February and 2022 January spectra which was not detectable in the 2020 December

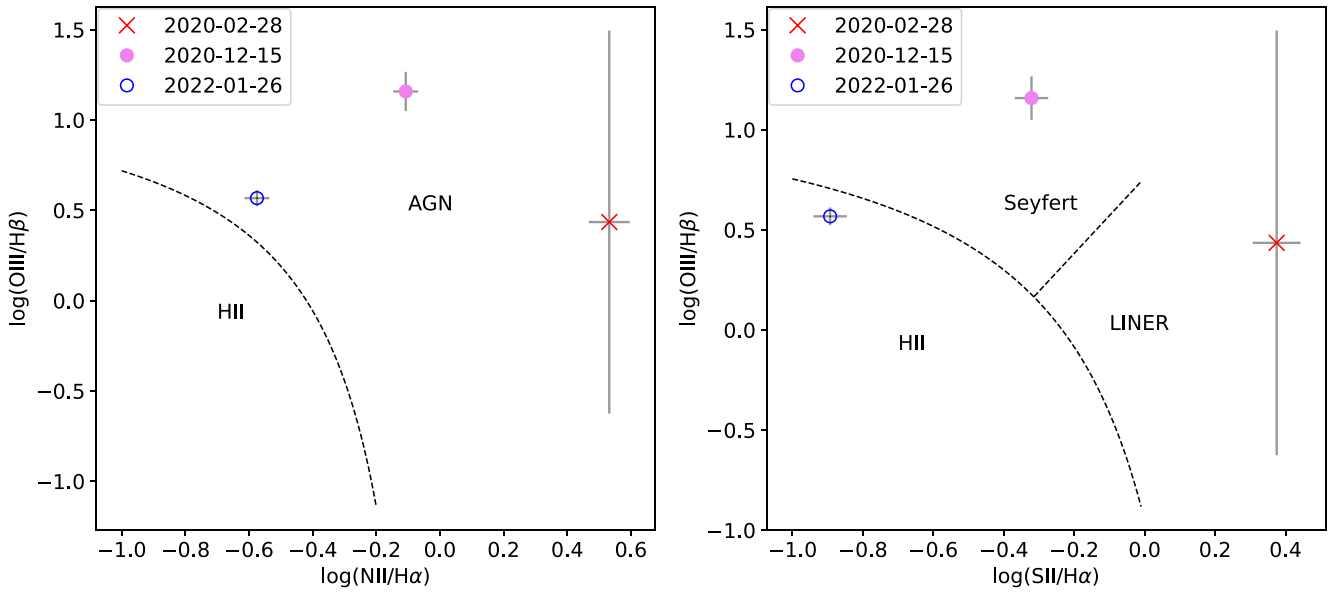

Figure 5. BPT diagrams showing the location of the nuclear emission in both our spectra. Measurements from the 2020 December spectrum clearly suggest the emission is due to an AGN, but the 2022 January emission lines more closely resemble a star-forming region. However, H β could be overestimated if there is an unresolved component from the TDE.

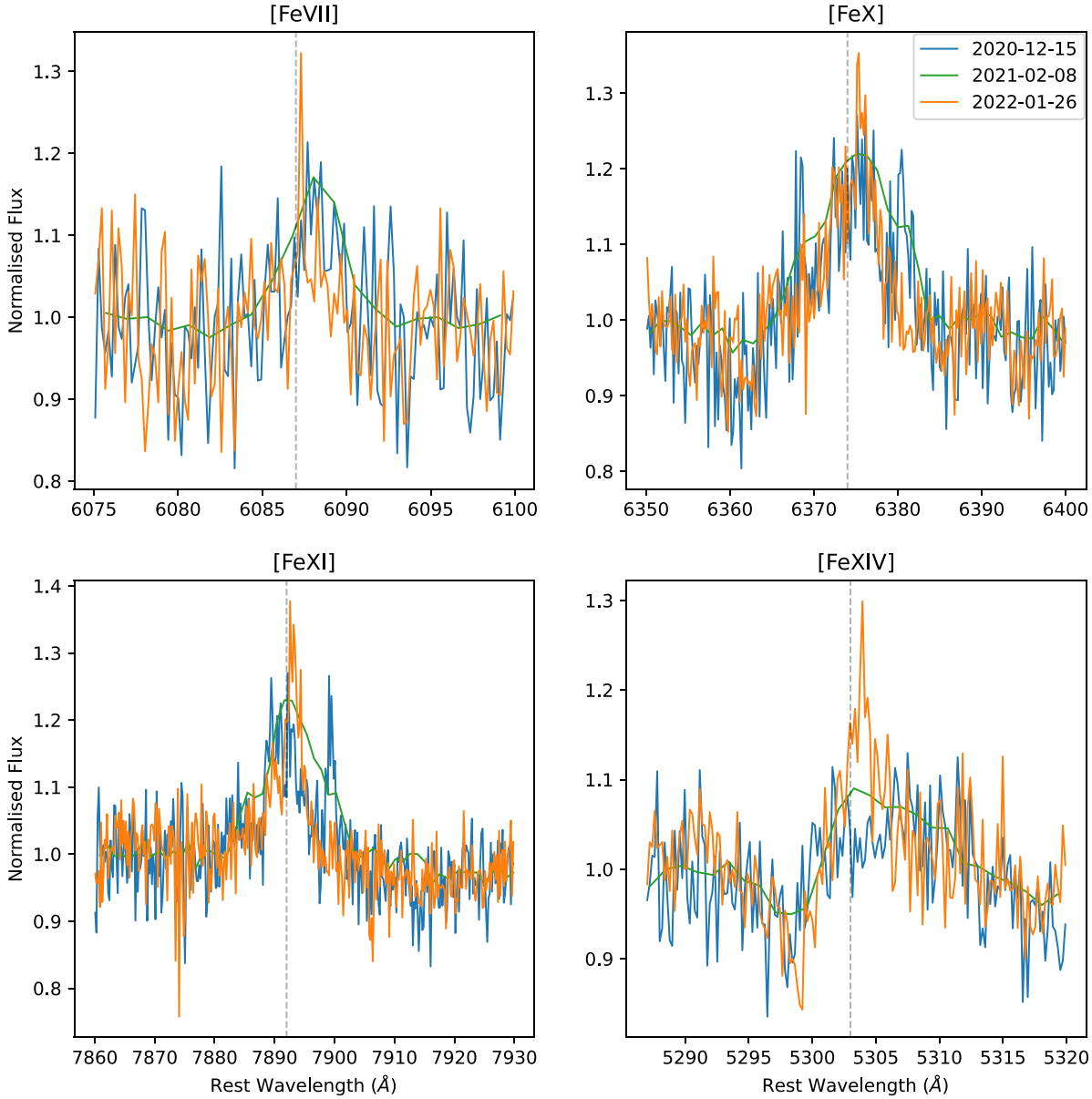

Figure 6. Comparison of Fe coronal line regions in all of our late-time spectra. The dotted grey line marks the rest-frame wavelengths of each line. The green spectrum is the MUSE spectrum, the orange and blue spectra are the X-Shooter data.

observation. We also note that in the 2020 December spectrum narrow features are visible either side of [Fe X] and redwards of [Fe XI]. A feature is also resolved redwards of [Fe X] in the 2021 February spectrum but the feature is not resolved in the [Fe XI] region. To determine whether or not these features are related we overplot the 2020 December lines in velocity space as shown in Fig. 7. Here, we can see that the red narrow features overlap. The red feature is displaced by $\sim$260 km s^{-1} from the line centre, while the blue feature is displaced by ~ -300 km s^{-1}. That the red feature is offset by a similar velocity in both the [Fe X] and [Fe XI] regions suggests that these features are from the same material. We investigated whether these features lined up with the velocity offsets of the broad Gaussian components fit to the H α blend, but, as shown in Fig. 7, they clearly originate from a different region.

We estimate line fluxes by fitting Gaussian profiles as with the narrow lines above. We fit the offset narrow emission features separately, noting that these are typically unresolved. We also check for the presence of Fe lines in the earlier X-Shooter spectra (Nicholl et al. 2020) dating back to $\sim$35 d after light-curve peak. In most cases, the lines are not detected in which case we set an upper flux limit one standard deviation above the continuum flux level. The exception to this is [Fe XI] which does seem to appear at earlier times. In Fig. B3, we plot the [Fe XI] region for all of the spectra we used. A feature is visible at around the right wavelength in the earlier spectra during outburst, though it is weak, broad and slightly offset so it seems likely this is not real [Fe XI] emission. We also plot the rest of the Fe line regions in and Figs B1, B2 and B4. The full list of lines and their flux measurements and line widths is displayed in Tables A1 and A2. In Fig. 8, we plot the evolution of each Fe emission line. In general, the flux of each line increases between the first and second spectra, before decreasing in the most recent spectrum, with the exception of [Fe XIV] as it appears for the first time in the 2021 February spectrum

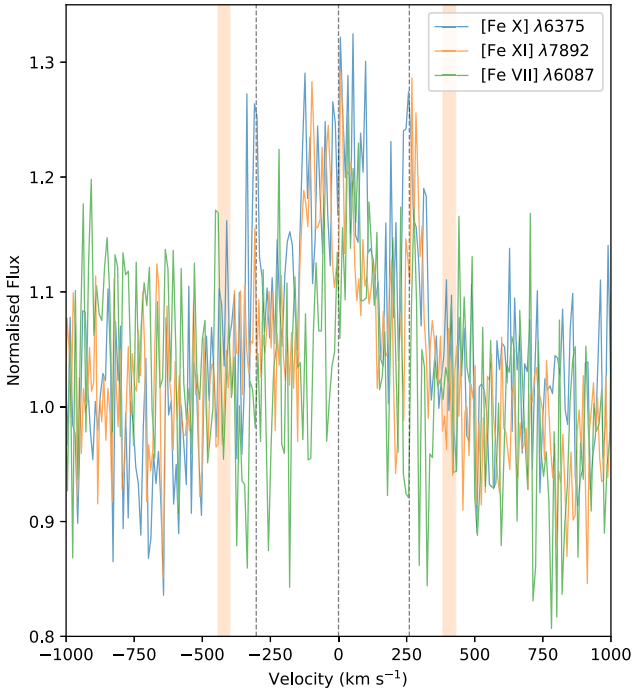

Figure 7. Fe lines in the 2020 December spectrum overplotted in velocity space. In the [Fe X], [Fe XI], and maybe [Fe VII] regions two features are visible, a broader component centred at 0 km s^{-1} and narrower line offset by ∼260 km s^{-1}. There is also a feature offset ∼300 km s^{-1} bluewards of [Fe X]. The grey dashed lines mark the line centres and the location of the offset components. The orange rectangles mark the locations of broad components fit to H α, where the widths cover $\pm 1\sigma$. These are offset much more than the narrow Fe features, showing they do not originate from the same region.

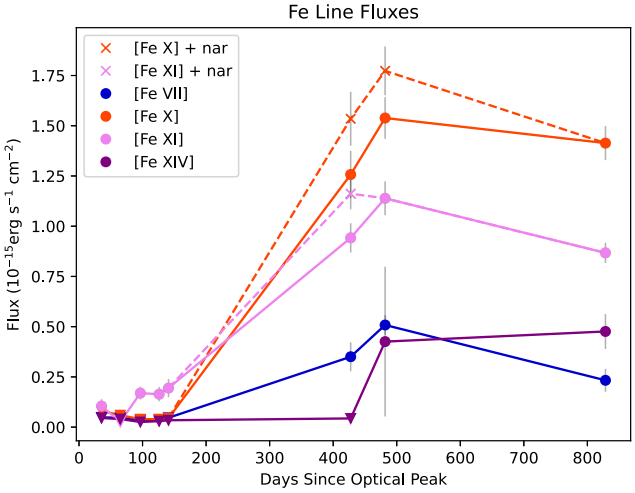

Figure 8. Evolution of Fe line fluxes since early outburst spectra. In cases where we do not detect a line we set 1σ upper limits denoted by the triangles. We include measurements from the 2020 December, 2022 February, and 2021 January spectra both with and without the narrow offset features. Measurements with narrow features are marked with crosses and dashed lines.

and increases in the 2022 January spectrum. The large errorbar in [Fe XIV] flux in the 2021 February spectrum comes from the fact that the line is not well resolved by MUSE. However, from Fig. 6 there does appear to be an increase in flux in this region compared to 2020 December. Wang et al. (2012) also observe evolution in the Fe line flux of their coronal line emitting objects. They carry out spectroscopic follow-up of three of their targets, taken several years after the first spectrum. They find that the [Fe X], [Fe XI], and [Fe XIV] flux decreases, but that the [Fe VII] flux remains constant.

The velocity widths of the highly ionized lines range from ∼150 to ∼300 km s^{-1}, with additional unresolved or barely resolved offset components in [Fe X] and [Fe XI]. In Section 7, we discuss what this implies for the structure and origin of the illuminated gas in AT2019qiz. Here, as with the low ionization lines, we examine whether the kinematic information is consistent with the flux evolution. If we once again use a 'virial distance', we find the coronal line material in the range of 50–300 light days. This is qualitatively consistent with the coronal line response peaking well before the low ionization lines. Quantitatively, it is not quite in simple agreement with observed flux peak at ∼500 d, and may suggest somewhat subvirial velocities, but a proper spatial and kinematic model would be needed before making any stronger statement.

4 X-RAY ANALYSIS

AT2019qiz is well detected in our new *Swift* XRT observation. We analyse the X-ray spectrum using XSPEC (Arnaud 1996), and compare it to the stacked XRT spectrum from the time of the optical peak (mean observation date 2019-11-07). We consider two models: a power-law spectrum, and a thermal model consisting of blackbody spectra summed over the annuli of an accretion disc. We initially include both Galactic absorption, determined using the maps from HI4pi (HI4PI Collaboration 2016) and intrinsic absorption in the host galaxy. However, for all models/epochs, we found an intrinsic column consistent with zero, and therefore exclude this from our final fits for simplicity. In the language of XSPEC, our models are therefore TBABS×ZPOWERLAW and TBABS×ZASHIFT×DISKBB, where TBABS is the Tübingen-Boulder ISM absorption model (Wilms, Allen & McCray 2000). We fit the data using the Cash statistic (Cash 1979). The fit parameters and derived fluxes for these models are given in Table 1.

Both models provide an adequate fit to the data, with reduced $\chi^2 \approx 1$. The thermal disc fits are shown compared to the data in Fig. 9. Regardless of which model is the more accurate physical description, we find an emphatic change in the spectral slope between the 2019 and 2022 observations. The new data show a much softer spectrum, with an inner disc temperature ∼0.1 keV (or a photon index ∼5), compared to an almost flat spectrum in 2019. The soft (0.3−1 keV) X-ray flux has increased by more than an order of magnitude, from $\sim 10^{-14}$ erg cm^{-2} s^{-1} in 2019 to $\gtrsim 5 \times 10^{-13}$ erg cm^{-2} s^{-1} in 2022, while the hard (1−6 keV) X-rays have fallen by a factor of several. We tested whether this could simply occur as a result of a decrease in absorption, by including intrinsic absorption in our models at the redshift of AT2019qiz (ZTBABS) and fitting the 2019 data with the temperature or photon index fixed to their best-fitting values for the 2022 data. However, this resulted in poor fits, suggesting that the underlying continuum (and not simply the degree of absorption) has changed between 2019 and 2022.

5 OUTBURST SED

The fluxes of narrow lines at 1–2 light-years from the SMBH reflect the ionizing continuum produced 1–2 yr earlier, i.e. the time of the optical peak. This allows us to construct a full SED of the initial flare using constraints from both the early and late-time data, filling in regions that could not be studied in earlier works. In Fig. 10, we

Table 1. Parameters and fluxes from X-ray model fits.

Parameter[a]	Power-law (TBABS×ZPOWERLAW) 2019	Power-law (TBABS×ZPOWERLAW) 2022	Thermal disc (TBABS×ZASHIFT×DISKBB) 2019	Thermal disc (TBABS×ZASHIFT×DISKBB) 2022
Γ (photon index)	1.13 ± 0.26	5.44 ± 1.12		
$k_B T_{in}$ (keV)			2.54 ± 1.25	0.13 ± 0.01
Normalization[b]	$(8.3 \pm 2.1) \times 10^{-6}$	$(4.9 \pm 1.5) \times 10^{-5}$	$(1.2 \pm 1.9) \times 10^{-4}$	272 ± 151
Unabsorbed flux in rest-frame (erg cm^{-2} s^{-1})				
0.3−10 keV	1.1×10^{-13}	6.9×10^{-13}	9.4×10^{-14}	5.2×10^{-13}
0.3−1 keV	1.0×10^{-14}	6.6×10^{-13}	7.4×10^{-15}	5.1×10^{-13}
1−6 keV	5.8×10^{-14}	2.4×10^{-14}	6.0×10^{-14}	9.7×10^{-15}

Notes. [a]Redshift fixed at $z = 0.0151$ and Galactic column density $n_H = 6.6 \times 10^{20}$ cm^{-2}. Any additional intrinsic column density in the host galaxy (modelled using ZTBABS) is found to be negligible and unconstrained in both models.
[b] Normalization is defined differently for power-law and disc models; see XSPEC documentation for details.

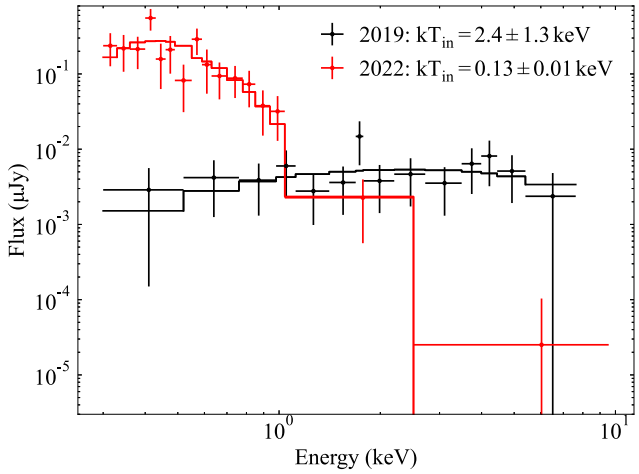

Figure 9. Our 2022 XRT spectrum (red) compared to the earlier 2019 observation (black; Nicholl et al. 2020). Both spectra can be adequately fit by power law or thermal disc models (DISKBB in XSPEC). The fit parameters are given in Table 1. The latter models have been used here to convert counts to fluxes, and are shown in the figure labelled by the temperatures at the inner disc edge. The softening of the spectrum is clearly visible.

attempt to construct the full SED of AT2019qiz during outburst. We use ZTF and UVOT photometry observed around MJD = 58794 to coincide with the effective date of the 2019 XRT spectrum. The data, reduced by Nicholl et al. (2020), were collected from TDE.space[4] (Guillochon et al. 2017). The infrared (IR) points are NEOWISE data (see Section 6) taken 92 d after the rest of the SED. The 13.6−54 eV power law was determined from the He II/H β ratio as discussed in Section 3.2 and scaled to be consistent with UVOT photometry. Both the 2019 and 2022 XRT spectra are included in this plot. The 2019 spectrum shows the X-ray flux during outburst and the 2022 spectrum shows how the increase in soft X-ray flux leads to the appearance of the Fe lines, whose ionisation potentials are marked on the plot. Fig. 10 highlights how the photons ionising the coronal lines fill the EUV gap between the He II ionizing photons and soft X-rays.

6 INFRARED ANALYSIS

AT 2019qiz is well detected in both *W*1 and *W*2 bands (3.4 and 4.6 μm, respectively) for 4 epochs of NEOWISE data. The host is well detected and non-variable in NEOWISE until the first detection of AT 2019qiz at MJD 58 886, 122 d after the optical peak derived in Nicholl et al. (2020). The IR fluxes then continue to increase until the most recent observation, 694 d after the optical peak at MJD 59458, although there is a slight decline in flux between the second and third observations. We calculate the flux solely due to the transient by subtracting the mean flux value detected from the galaxy before the first detection, and the corresponding magnitudes are shown in the top panel of Fig. 11. The flux at 3.4 μm from the UV/optical blackbody of AT 2019qiz at the epoch of the first IR detection, calculated using the temperature and radius values given in Nicholl et al. (2020), is ∼0.5 per cent of the observed host-subtracted W1 flux, and so negligible. Therefore, we interpret the IR detections shown here as an IR echo from dust in the vicinity of the SMBH, similarly to those observed in a number of other optical-UV TDEs (see e.g. van Velzen et al. 2016; Jiang et al. 2021).

We estimated the BB parameters for the IR echo using the EMCEE PYTHON implementation of the Markov Chain Monte Carlo (MCMC) method (Foreman-Mackey et al. 2013) to fit the host-subtracted fluxes and derive uncertainties (as described in Reynolds et al. 2022). The resulting parameters are shown in the middle panel of Fig. 11. The temperature measured in the first observation, $T_{max} = 1450^{+90}_{-80}$ K, is close to, although slightly lower than, the sublimation temperature for astrophysical dust, which typically lies between 1500 and 2000 K depending on the composition of the dust (see e.g. Waxman & Draine 2000; Lu, Kumar & Evans 2016; van Velzen et al. 2016). We note that the inferred radii do not directly correspond to the distance from the SMBH to the dust, and we do not necessarily expect a spherical shell, but do provide a lower limit.

We estimate the luminosity of the IR echo at each epoch from the temperature and radius parameters using the Stefan–Boltzmann law, and integrate the luminosity evolution from the first to the last detection to estimate the total radiated energy of the IR echo to date. The luminosity is highest in the most recent observation, where the luminosity is 3.2×10^{42} erg s^{-1}, and the total radiated energy up until this point is 1.20×10^{50} erg. If we calculate the covering factor by comparing the peak luminosity for the UV/optical blackbody [3.6×10^{43} erg s^{-1}, Nicholl et al. (2020)] to the peak in the IR, similarly to Jiang et al. (2021), we find a lower limit for the covering factor of $f_c = L_{dust,\,peak}/L_{opt+UV,peak} = 0.09$, assuming the IR fluxes are still rising. This is considerably higher than the values found for the sample of optical TDEs in Jiang et al. (2021), where the covering factor was typically ∼0.01. We can additionally consider the definition of the covering factor given in van Velzen et al. (2021a), $\Omega_d = E_{bol}/E_{dust}$, where E_{bol} and E_{dust} are the total radiated energy of the TDE (integrated over the wavelength where dust absorption is

[4]https://tde.space/

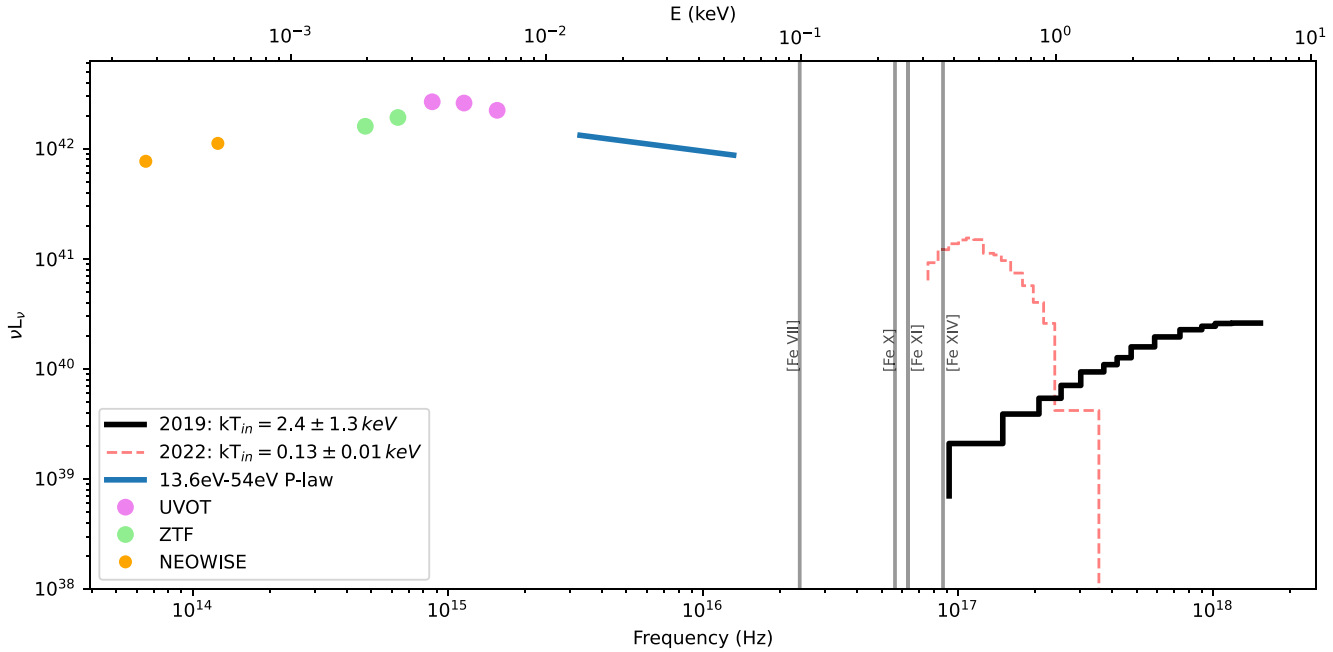

Figure 10. The full SED of AT2019qiz in outburst on MJD ∼58794. The more recent XRT spectrum is also included to highlight the jump in soft X-ray flux. The IR points are for the first detection on MJD 58886, 92 d after the rest of the SED. Error bars in the photometry points are too small to be seen on this scale.

efficient) and the dust, respectively. If we estimate the total radiated energy of the TDE with the value obtained from the UV/optical bolometric LC by Nicholl et al. (2020), 1.0×10^{50} erg, we find $\Omega_d = 0.84$, i.e. an approximate equipartition of the radiated energy between the IR echo and the prompt UV/optical emission. Although the total energy radiated given in Nicholl et al. (2020) only measures until ∼150 d, if we conservatively assume that the TDE has remained at the same bolometric luminosity from that point until the most recent IR observation, the total radiated energy would only increase by ∼20 per cent, so the value of Ω_d will not be greatly affected. Furthermore, the IR emission is still rising. In summary, the IR echo observed for AT 2019qiz is exceptionally luminous for a TDE discovered in the optical. We discuss this, and the connection to the IR echo observed for AT 2017gge, in Section 7.

7 DISCUSSION

We examine the implications of our results for several key issues – the true TDE continuum, the structure and origin of the material surrounding the TDE, and the relation of this object to other coronal line emitters. First, however, we discuss whether AT2019qiz was truly a TDE, as opposed to an SN, or an AGN outburst.

7.1 TDE, SN, or AGN?

The optical spectrum of the outburst of AT2019qiz fits solidly into the standard class of optical-UV TDEs, but its absolute magnitude at peak, $R_{pk} \sim -19$, was somewhat towards the lower end of the range for such objects (Nicholl et al. 2020), overlapping the range of typical SNe. At the same time, the low-ionization line ratios seen in outburst (Nicholl et al. 2020) suggest some weak AGN-like activity in the past.

Could AT2019qiz actually be a kind of SN? The delayed appearance of coronal lines has been seen in a handful of SNe – for example SN1988z (Aretxaga et al. 1999), SN2005ip (Smith et al. 2009, 2017), and SN1987A (Gröningsson et al. 2006); see also discussion in Komossa et al. (2009). Such objects are clearly extremely rare – out of the thousands of SNe seen so far, only a handful have developed coronal lines. This phenomenon seems to require earlier mass-loss to produce significant amounts of circumstellar material; following the outburst, shocks from the blast wave make X-ray emission that then produces the coronal lines. The delay is due to blast wave travel time, not light travel time, and the coronal lines can persist for quite a long time (see references above). For the original TDE light echo candidate, J0952 + 2143, Komossa et al. (2009) were able to argue against an SN origin, because the observed [Fe VII] luminosity was 1.6×10^{40} erg s^{-1}, two orders of magnitude larger than for these rare extreme SNe. For AT2019qiz however, the [Fe VII] luminosity is 3.4×10^{38} erg s^{-1}, not so far from what was seen in SN2005ip, 1.5×10^{38} erg s^{-1} (Smith et al. 2009). Purely on luminosity grounds, we cannot rule out an SN origin. The outburst optical spectrum of AT2019qiz was not quite like any of these extreme SNe – for example, SN2005ip and SN1988z show lines to the red of H α such as the Ca triplet which have never been seen in a TDE. However, SN spectra are diverse enough that we cannot strictly rule out an SN origin on this basis either, if we consider AT2019qiz in isolation. However, the similarity of AT2019qiz to other optical-UV TDEs suggests that if we explain AT2019qiz as an SN, we should consider this possibility for all TDEs, including the more luminous ones. We would also need to explain why these particular characteristics are only found in the centres of galaxies with black holes in the range of 10^6–10^7 $M_\odot$.

Could the AT2019qiz outburst be due to some kind of AGN activity, rather than a tidal disruption? In both scenarios, we assume the existence of an SMBH, and an enhanced period of accretion, so that the ionizing continuum is likely much the same in either case (see Section 7.2). The key question then is the nature and origin of the surrounding material, which we discuss in Sections 7.3 and 7.4. A lack of pre-existing material would argue for a completely dormant black hole, as opposed to a passive disk around the black

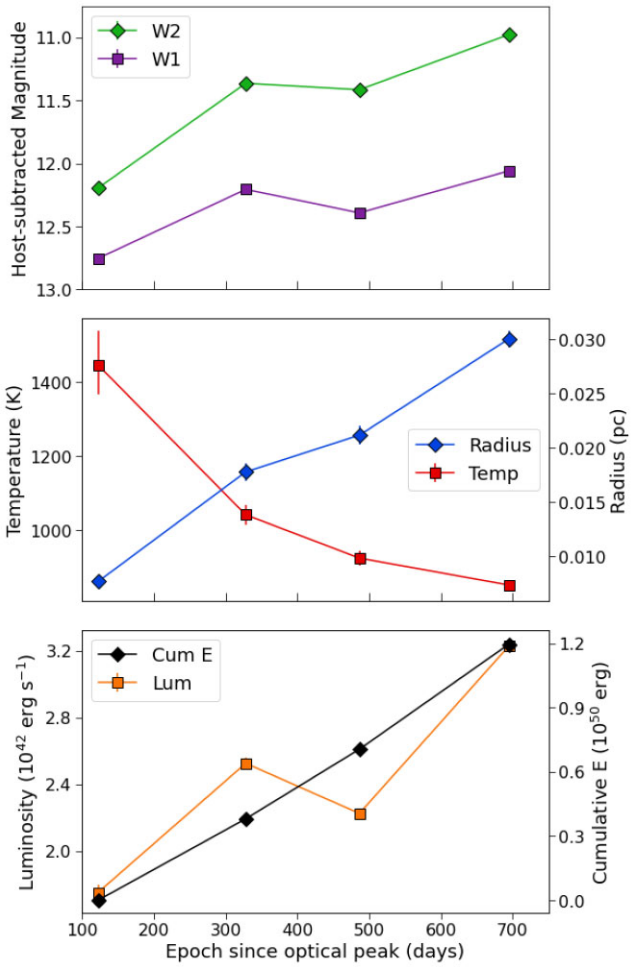

Figure 11. Top: Host subtracted magnitudes for NEOWISE observations of AT 2019qiz. Middle: Temperatures and radii inferred from blackbody fitting of the host subtracted fluxes of AT 2019qiz. Bottom: Luminosities implied by the blackbody parameters and the cumulative energy implied by those luminosities.

hole. However of course, it is quite possible for a stellar disruption to take place in the presence of a passive disc.

7.2 Existence of a hard continuum

The coronal lines almost certainly result from photo-ionization – the very high gas temperatures required mean that collisional ionization would predict line widths of thousands rather than hundreds of km s^{-1}. The high ionization coronal lines are then direct evidence of a hard EUV continuum. While He II and Bowen line emission also require an EUV source, the coronal lines have significantly higher ionization potentials from ∼100 eV up to nearly 400 eV in the case of [Fe XIV]. We also find a very soft X-ray spectrum which further hints at the presence of an unobservable continuum. The existence of continuum emission in this energy range is significant as it is predicted by accretion models but is not directly observed. Typical blackbody temperatures observed in TDEs are of order 10^4 K, which is generally assumed to be reprocessed emission from the true, harder continuum that peaks in the EUV. The detection of coronal lines proves this harder continuum emission exists, and must somehow escape the reprocessing region, perhaps because of either clumpiness, or a non-spherical geometry. In principle, the complete set of emission lines can constrain the shape of the EUV continuum, and the covering factor of illuminated material, but such modelling is beyond the scope of this paper.

7.3 Structure of the surrounding material

The Fe line light curves in Fig. 8 give us the first clues about the geometry of the surrounding structure. The decline of the Fe light curve is much slower than that of the continuum, so must be convolved with a broad response function. This can be caused either by a spread in light travel times due to a range of radial distances, or due to reflection from material at different angles to our line of sight, or both. Physical models of different reprocessing region geometries produce different response functions (e.g. Perez, Robinson & de La Fuente 1992), but unfortunately our sparsely populated light curves make it difficult to compare. The lack of a prompt response to the original outburst tells us there is little material along our line of sight, although another source of uncertainty is whether the coronal lines are responding to the initial outburst or the more recent increase in soft X-ray flux.

Inconsistent ionization parameter changes also show there is a complex structure surrounding the SMBH. [Fe XIV] appears in the 2021 and 2022 spectra despite not being observed previously. The other Fe lines decrease in flux after the 2021 spectrum. We also see a significant rise in the flux of narrow lines such as the Balmer lines, [N II] and [S III]. The changes in the strengths of different emission lines require differing ionization parameters, which depends on the density of the emitting gas. The later appearance of [Fe XIV] could imply low density material further from the SMBH (therefore with a greater light travel time), or alternatively higher density material closer to the SMBH, but behind the nucleus from our point of view. Even further from the black hole, there must be material with a low ionization parameter, thus emitting strongly in H α, H β, and other low ionization lines. What is not clear is why the narrow Balmer lines get broader in the second spectrum. In addition the move in the BPT diagrams (Fig. 5) from obvious AGN emission to something more closely resembling a star forming region is puzzling. Both could be a sign of an increasing contribution to the narrow lines from the TDE emission, causing both a broadening of the narrow lines and altering their ratios by changing the ionizing continuum. The jump in broad-line flux in the 2021 January spectrum could be further evidence for a complex structure. The structure surrounding the black hole may be made up of clumpy material, in which case the obscuration of the central region may fluctuate. If the broad emission line originates from an accretion disc, then the increase in flux could be due to there being less material obscuring our line of sight to the disc.

The combination of large dust covering factors and coronal Fe lines observed for both AT2019qiz and AT2017gge suggests a connection between the phenomena. Additionally, AT 2019avd also exhibited a very high dust covering factor with f_c ∼0.5 (Chen et al. 2022) along with displaying coronal lines. In particular, the coronal Fe lines could arise from Fe that was locked in dust grains that were destroyed by the UV emission from the TDE. This would be similar to the case of Coronal Line Forest AGNs, where it has been suggested that the coronal lines could be produced in the inner wall of the dusty torus, where the AGN is sublimating the dust (Rose, Elvis & Tadhunter 2015). In the case of AT 2019qiz, both Hung et al. (2021) and (Nicholl et al. 2020) note that there is likely to be a low luminosity AGN within the host galaxy of AT 2019qiz. The AGN unification model suggests the presence of a dusty obscuring structure, a torus, which here could be responsible for both the IR echo and potentially the coronal lines. The luminosity of the TDE in the UV/optical and lack

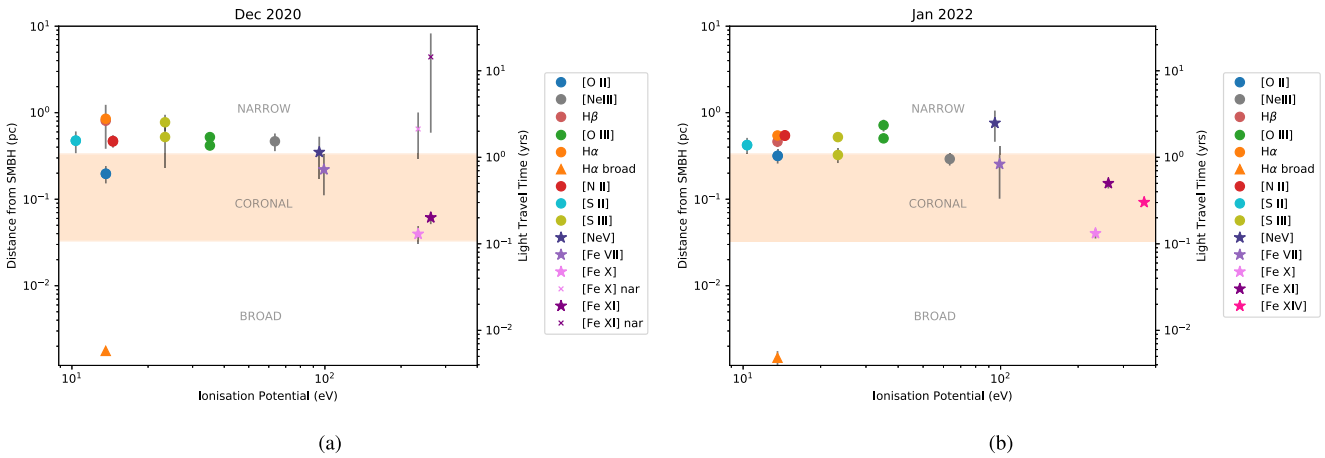

(a) (b)

Figure 12. The estimated distance of the gas emitting various line species, plotted against their ionisation potential. The estimated distance is based on equating the (corrected) FWHM of the line with the expected virial velocity for a 10^6 $M_\odot$ SMBH. Based on these measurements we label narrow, coronal and broad line regions.

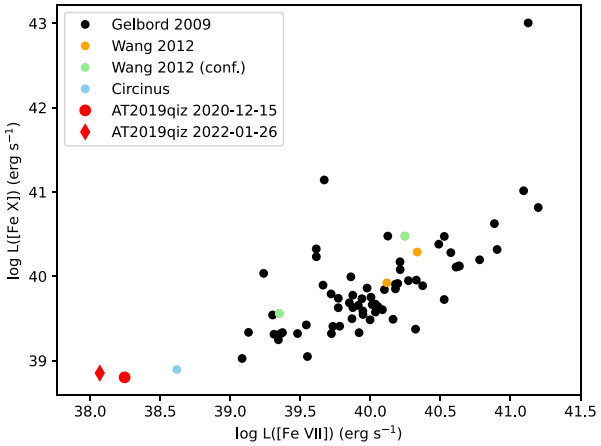

(a)

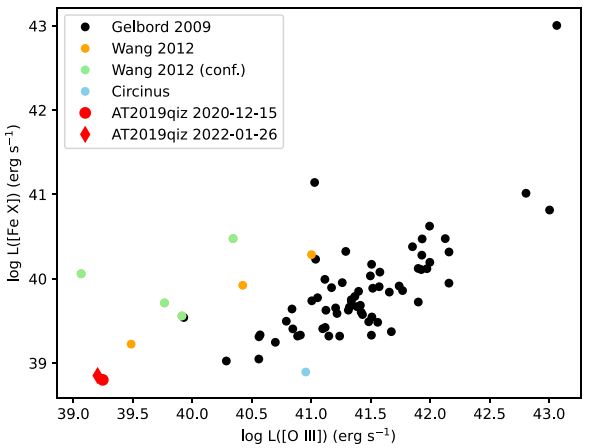

(b)

Figure 13. A comparison of line ratios with other coronal line emitting objects. The light green points are the four objects in the Wang et al. (2012) sample that were confirmed to have variable coronal lines by Komossa et al. (2008) and Yang et al. (2013). Interestingly, in Fig. 13(b) AT2019qiz looks more in keeping with suspected TDEs.

of evidence for significant extinction implies that the dust producing the IR echo is not substantially in the observer line of sight, which could additionally imply an unobscured line of sight to the inner dusty regions that Rose et al. (2015) argue is required to observe the coronal lines. The AGN associated dust structures additionally explain the high covering factor in AT 2019qiz compared to the optical TDE sample, which are almost all in galaxies that do not host an AGN. This is supported by comparison to TDEs and TDE candidates that have been observed in galaxies that host AGN such as Arp 299-B AT1 (Mattila et al. 2018; Reynolds et al. 2022), AT 2017gbl (Kool et al. 2020), and ASASSN-15lh (Krühler et al. 2018), which also display very energetic IR echoes, as indeed does the original TDE echo candidate J0952 + 2143 (Komossa et al. 2009). There is no unambiguous evidence for either AT 2017gge or AT 2019avd hosting an AGN before undergoing their nuclear outbursts, but it also cannot be ruled out.

Our observations show that in AT2019qiz, the continuum emission must be reprocessed at a range of distances. The Fe line profiles are irregular with disappearing offset components. The observed emission lines also have a range of widths, with the coronal lines generally being broader than the low ionization narrow lines. We can use our 'virial distance' estimates (see Section 3.2) to examine the stratification of the material surrounding the outburst event. Fig. 12 shows estimated distance versus ionization potential for various observed lines, for each of the two X-Shooter epochs. We can divide material loosely into 'broad line,' 'coronal line,' and 'narrow line' regions, but even the coronal line region seems to show ionization stratification. To go beyond this statement would require a full model, beyond the scope of this paper. Furthermore, as discussed in Section 3.2, the distance estimates may be an underestimate because the gas motion is responding to the galaxy potential as well as the black hole. The key point however is that the low-ionization narrow lines are clearly narrower than the coronal lines.

7.4 Origin of the surrounding material

We have seen that the material causing the IR echo must have a large covering factor and so seems much more likely to be connected with the nuclear activity, rather than being random interstellar material. Assessing the amount of material responsible for the coronal lines is not trivial, as it is rather model independent. Detailed modelling

is underway (Yin et al. in preparation) but for any reasonable SED, placing material at the relevant critical density, and at a distance corresponding to the observed delay time, indicates that likewise a significant covering factor is required to reproduce the line flux, of the order 1–10 per cent.

Furthermore, the illuminated material is too far from the black hole to have been expelled from the 2019 outburst. We do not have a kinematic model, but the outflow time will likely be of the order of the dynamical timescale $t = \sqrt{R^3/GM}$. If we place the [Fe X] material at the light echo distance based on the light curve peak at 500 d, the outflow time is ∼4000 yr. The outflow time to the Balmer lines, still rising at 800 d, is at least ∼8200 yr. Even at relativistic jet-like outflow velocities, the outflow cannot outpace the illuminating light. The material could have been placed there by previous AGN activity, or the host could have significant amounts of gas along the line of sight. Intriguingly, if we were to speculate that the material is the remnant of a previous TDE, the dynamical timescale would be consistent with the expected average TDE rate of $\sim 10^{-4}$ yr^{-1} galaxy^{-1}. Whether or not a past TDE would leave enough material to produce the observed line luminosities, or indeed which of these scenarios is most likely, is left for future work to investigate.

7.5 Comparison to other coronal line emitters

AT2019qiz and very recently AT2017gge (Onori et al. 2022) are the only spectroscopically confirmed optical-UV TDEs to have developed coronal lines and it is not clear why this is the case. The Dec 2020 spectrum was obtained as part of a study of TDE host galaxies, and was thus one of a sample of other 'very late time' TDE spectra. Out of the 11 objects in our sample AT2019qiz was the only one to show signs of Fe lines, despite some of the other host galaxies also hosting AGN. Out of our sample of late time TDE spectra, AT2019qiz was the most recent, and it is also one of the most nearby TDEs discovered to date. It could be that these coronal lines have been produced in other TDEs but simply have not been detected. However, AT2017gge (Onori et al. 2022) is significantly further away at $z = 0.0665$ and the coronal lines were still detected 1700 d after the initial outburst. It remains unclear what is special about AT2019qiz or AT2017gge.

Coronal lines are common in AGN (Oliva et al. 1994; Gelbord et al. 2009) and of the class of ECLEs, several are strongly suspected to be light echos from past TDEs (Komossa et al. 2008; Wang et al. 2011, 2012). In Fig. 13, we compare AT2019qiz with some of these coronal line emitters from the literature on plots of [Fe X] versus [Fe VII] and [Fe X] versus [O III] λ5007. The comparison sample is made up of coronal line AGN from Gelbord et al. (2009), a nearby Seyfert 2 (the *Circinus* galaxy) from Oliva et al. (1994) and the possible TDEs from Wang et al. (2012) (Note that we have separated the four galaxies (SDSS J0952+2143, SDSS J1241+4426, SDSS J0748+4712, and SDSS J1350 + 2916) which had confirmed highly variable coronal lines through follow-up spectra). In both plots, there is a correlation between the line ratios which is a sign that the lines are photoionized rather than collisionally ionized. In Fig. 13(b), the Wang et al. (2012) objects appear to follow a different correlation to the Gelbord et al. (2009) AGN. Interestingly, AT2019qiz is more consistent with the Wang et al. (2012) objects than the AGN, albeit at lower luminosity than all the others. This likely confirms the speculation of Komossa et al. (2008) and Wang et al. (2012) that the coronal lines in many of these objects are remnants of a TDE outburst. Based on their sample, Wang et al. (2012) estimate an event rate for coronal line emitters of $\sim 10^{-5}$ galaxy^{-1} yr^{-1}. In our sample of very late time TDE spectra, only ∼ 10 per cent of events develop coronal lines. This is consistent with TDE rate estimates (Donley et al. 2002; Wang & Merritt 2004; Kesden 2012), though we acknowledge the caveats that (a) our sample size is small and (b) the spectra were obtained at different epochs relative to initial outburst of each event.

8 CONCLUSION

AT2019qiz is the clearest example to date of a spectroscopically confirmed optical-UV TDE developing high ionisation coronal lines in its spectra, appearing ∼400 d after the main optical flare. These lines are direct evidence for the presence of a hard EUV continuum. The lines originate from a pre-existing, complex surrounding structure with different ionization potentials in different regions. Aside from AT2017gge, no other confirmed optical-UV TDEs to date have shown coronal line emission, but the line ratios of AT2019qiz are consistent with coronal line emitters from the literature which are suspected to be TDE remnants. In addition, the estimated rate of coronal line emitters is consistent with the estimated rate of TDEs and the fraction of our late time TDE sample which develop coronal lines. The IR echo observed from AT2019qiz, along with other coronal line emitters, is notably more luminous than typical for optical TDEs, and suggests a connection between these phenomena. This could be explained through the coronal lines arising from Fe liberated from dust grains that were destroyed by the TDE flare. Future studies should systematically search for coronal line emission in late time TDE spectra.

ACKNOWLEDGEMENTS

MN is supported by the European Research Council (ERC) under the European Union's Horizon 2020 research and innovation programme (grant agreement no. 948381) and by funding from the UK Space Agency. MJW acknowledges support of a Leverhulme Emeritus Fellowship, EM-2021-064, during the preparation of this paper. TMR acknowledges the financial support of the Vilho, Yrjö and Kalle Väisälä Foundation of the Finnish academy of Science and Letters. SM acknowledges support from the Academy of Finland project 350458. IA is a Canadian Institute for Advanced Research (CIFAR) Azrieli Global Scholar in the Gravity and the Extreme Universe Program and acknowledges support from that programme, from the European Research Council (ERC) under the European Union's Horizon 2020 research and innovation program (grant agreement number 852097), from the Israel Science Foundation (grant number 2752/19), from the United States – Israel Binational Science Foundation (BSF), and from the Israeli Council for Higher Education Alon Fellowship. AC would like to thank the Leverhulme Trust for their support via the Leverhulme Early Career Fellowship scheme. PC and GL are supported by a research grant (19054) from VILLUM FONDEN. MG is supported by the EU Horizon 2020 research and innovation programme under grant agreement no. 101004719. FO acknowledges support from the Italian Ministry of Education, University and Research (MIUR), Research Projects of National Relevance (PRIN) 2017 (grant 20179ZF5KS) 'The new frontier of the Multi-Messenger Astrophysics: follow-up of electromagnetic transient counterparts of gravitational wave sources' and the support of HORIZON2020: AHEAD2020 grant agreement no. 871158. For the purpose of open access, the author has applied a Creative Commons Attribution (CC BY) licence to any Author Accepted Manuscript version arising from this submission.

DATA AVAILABILITY

All spectra will be made available on WISeREP (https://www.wiserep.org/) upon acceptance of the paper. *Swift* NEOWISE data are already publicly available.

REFERENCES

Adelman-McCarthy J., 2008, ApJS, 175, 297
Arcavi I. et al., 2014, ApJ, 793, 38
Aretxaga I., Benetti S., Terlevich R. J., Fabian A. C., Cappellaro E., Turatto M., della Valle M., 1999, MNRAS, 309, 343
Arnaud K. A., 1996, in Jacoby G. H., Barnes J., eds, ASP Conf. Ser. Vol. 101, Astronomical Data Analysis Software and Systems V. Astron. Soc. Pac., San Francisco, p. 17
Auchettl K., Guillochon J., Ramirez-Ruiz E., 2017, ApJ, 838, 149
Bacon R. et al., 2010, in McLean I. S., Ramsay S. K., Takami H., eds, Proc. SPIE Conf. Ser. Vol. 7735, Ground-based and Airborne Instrumentation for Astronomy III. SPIE, Bellingham, p. 773508
Baldwin J. A., Phillips M. M., Terlevich R., 1981, PASP, 93, 5
Breeveld A. A., Landsman W., Holland S. T., Roming P., Kuin N. P. M., Page M. J., 2011, in McEnery J. E., Racusin J. L., Gehrels N., eds, AIP Conf. Ser. Vol. 1358, Gamma Ray Bursts 2010. Am. Inst. Phys., New York, p. 373
Cannizzaro G. et al., 2021, MNRAS, 504, 792
Cappellari M., 2017, MNRAS, 466, 798
Cash W., 1979, ApJ, 228, 939
Charalampopoulos P. et al., 2022, A&A, 659, A34
Chen J.-H., Dou L.-M., Shen R.-F., 2022, ApJ, 928, 63
Dai L., McKinney J. C., Roth N., Ramirez-Ruiz E., Miller M. C., 2018, ApJ, 859, L20
Donley J. L., Brandt W. N., Eracleous M., Boller T., 2002, AJ, 124, 1308
Evans P. A. et al., 2009, MNRAS, 397, 1177
Fitzpatrick E. L., 1999, PASP, 111, 63
Foreman-Mackey D., Hogg D. W., Lang D., Goodman J., 2013, PASP, 125, 306
Forster F., 2019, Transient Name Serv. Discovery Rep., 2019-1857, 1
Freudling W., Romaniello M., Bramich D. M., Ballester P., Forchi V., García-Dabló C. E., Moehler S., Neeser M. J., 2013, A&A, 559, A96
Gehrels N. et al., 2004, ApJ, 611, 1005
Gelbord J. M., Mullaney J. R., Ward M. J., 2009, MNRAS, 397, 172
Gezari S., 2021, ARA&A, 59, 21
Grandi S. A., 1978, ApJ, 221, 501
Gröningsson P., Fransson C., Lundqvist P., Nymark T., Lundqvist N., Chevalier R., Leibundgut B., Spyromilio J., 2006, A&A, 456, 581
Guillochon J., Manukian H., Ramirez-Ruiz E., 2014, ApJ, 783, 23
Guillochon J., Parrent J., Kelley L. Z., Margutti R., 2017, ApJ, 835, 64
Gültekin K. et al., 2009, ApJ, 698, 198
HI4PI Collaboration, 2016, A&A, 594, A116
Hills J. G., 1975, Nature, 254, 295
Hodgkin S. T., Wyrzykowski L., Blagorodnova N., Koposov S., 2013, Phil. Trans. R. Soc. London Ser. A, 371, 20120239
Hung T. et al., 2020, ApJ, 903, 31
Hung T. et al., 2021, ApJ, 917, 9
Jiang N., Wang T., Hu X., Sun L., Dou L., Xiao L., 2021, ApJ, 911, 31
Kauffmann G. et al., 2003, MNRAS, 346, 1055
Kesden M., 2012, Phys. Rev. D, 85, 024037
Komossa S., Bade N., 1999, A&A, 343, 775
Komossa S., Greiner J., 1999, A&A, 349, L45
Komossa S. et al., 2008, ApJ, 678, L13
Komossa S. et al., 2009, ApJ, 701, 105
Kool E. C. et al., 2020, MNRAS, 498, 2167
Kormendy J., Ho L. C., 2013, ARA&A, 51, 511
Krühler T. et al., 2018, A&A, 610, A14
Leloudas G. et al., 2019, ApJ, 887, 218
Loeb A., Ulmer A., 1997, ApJ, 489, 573
Lu W., Kumar P., Evans N. J., 2016, MNRAS, 458, 575
Mainzer A. et al., 2011, ApJ, 731, 53
Mainzer A. et al., 2014, ApJ, 792, 30
Malyali A. et al., 2021, A&A, 647, A9
Martin D. C. et al., 2005, ApJ, 619, L1
Mattila S. et al., 2018, Science, 361, 482
McConnell N. J., Ma C.-P., 2013, ApJ, 764, 184
Nicholl M. et al., 2019, MNRAS, 488, 1878
Nicholl M. et al., 2020, MNRAS, 499, 482
Nicholl M., Lanning D., Ramsden P., Mockler B., Lawrence A., Short P., Ridley E. J., 2022, MNRAS, 515, 5604
Oliva E., Salvati M., Moorwood A. F. M., Marconi A., 1994, A&A, 288, 457
Onori F. et al., 2022, MNRAS, 517, 76
Palaversa L., Gezari S., Sesar B., Stuart J. S., Wozniak P., Holl B., Ivezić Ž., 2016, ApJ, 819, 151
Penston M. V., Fosbury R. A. E., 1978, MNRAS, 183, 479
Penston M. V., Fosbury R. A. E., Boksenberg A., Ward M. J., Wilson A. S., 1984, MNRAS, 208, 347
Perez E., Robinson A., de La Fuente L., 1992, MNRAS, 256, 103
Petrushevska T. et al., 2023, A&A, 669, A140
Rees M. J., 1988, Nature, 333, 523
Reynolds T. M., Mattila S., Efstathiou A., Kankare E., Kool E., Ryder S., Peña-Moñino L., Pérez-Torres M. A., 2022, A&A, 664, A158
Rose M., Elvis M., Tadhunter C. N., 2015, MNRAS, 448, 2900
Roth N., Kasen D., 2018, ApJ, 855, 54
Roth N., Kasen D., Guillochon J., Ramirez-Ruiz E., 2016, ApJ, 827, 3
Schlafly E. F., Finkbeiner D. P., 2011, ApJ, 737, 103
Short P. et al., 2020, MNRAS, 498, 4119
Smith N. et al., 2009, ApJ, 695, 1334
Smith N. et al., 2017, MNRAS, 466, 3021
STScI Development Team, 2013, Astrophysics Source Code Library, record ascl:1303.023
van Velzen S., Mendez A. J., Krolik J. H., Gorjian V., 2016, ApJ, 829, 19
van Velzen S., Holoien T. W. S., Onori F., Hung T., Arcavi I., 2020, Space Sci. Rev., 216, 124
van Velzen S., Pasham D. R., Komossa S., Yan L., Kara E. A., 2021a, Space Sci. Rev., 217, 63
van Velzen S. et al., 2021b, ApJ, 908, 4
Veilleux S., Osterbrock D. E., 1987, ApJS, 63, 295
Vernet J. et al., 2011, A&A, 536, A105
Wang J., Merritt D., 2004, ApJ, 600, 149
Wang T.-G., Zhou H.-Y., Wang L.-F., Lu H.-L., Xu D., 2011, ApJ, 740, 85
Wang T.-G., Zhou H.-Y., Komossa S., Wang H.-Y., Yuan W., Yang C., 2012, ApJ, 749, 115
Wang Y. et al., 2022, ApJ, 930, L4
Waxman E., Draine B. T., 2000, ApJ, 537, 796
Weilbacher P. M. et al., 2020, A&A, 641, A28
Wevers T., van Velzen S., Jonker P. G., Stone N. C., Hung T., Onori F., Gezari S., Blagorodnova N., 2017, MNRAS, 471, 1694
Wevers T. et al., 2019a, MNRAS, 487, 4136
Wevers T. et al., 2019b, MNRAS, 488, 4816
Wevers T. et al., 2022, A&A, 666, A6
Wilms J., Allen A., McCray R., 2000, ApJ, 542, 914
Yang C.-W., Wang T.-G., Ferland G., Yuan W., Zhou H.-Y., Jiang P., 2013, ApJ, 774, 46

APPENDIX A: EMISSION LINE FIT RESULTS

Table A1. Results from Gaussian fits to emission lines in the 2020 December spectrum, after correction for instrumental resolution, which is approximately 56 km s^{-1} for blue arm lines, $\lambda < 5600$ Å, and 34 km s^{-1} for red arm lines, $\lambda > 5600$ Å. As discussed in the text, we estimate that line fluxes have an addition ∼15 per cent systematic error.

Line	Centre (Å)	Flux 10^{-16} (erg s^{-1}cm^{-2})	FWHM (km s^{-1})
[Ne V] λ3426	3426.27 ± 0.12	5.85 ± 1.16	106 ± 26
[O II] λ3727	3726.26 ± 0.15	4.46 ± 0.65	144 ± 16
[O II] λ3729	3729.48 ± 0.12	5.57 ± 0.68	143 ± 16
[Ne III] λ3869	3869.29 ± 0.05	4.99 ± 0.44	90 ± 10
Hβ	4862.15 ± 0.09	2.44 ± 0.61	65 ± 16
[O III] λ4959	4959.77 ± 0.03	10.06 ± 0.41	84 ± 4
[O III] λ5007	5007.59 ± 0.01	35.17 ± 0.62	96 ± 2
[Fe VII] λ6087	6088.25 ± 0.28	3.5 ± 0.72	143 ± 33
[Fe X] λ6375	6374.63 ± 0.27	12.57 ± 1.18	330 ± 38
[Fe X] off	6380.72 ± 0.16	2.78 ± 0.63	86 ± 20
[N II] λ6549	6549.74 ± 0.19	2.78 ± 0.2	100 ± 7
H α n	6563.83 ± 0.03	10.69 ± 0.57	77 ± 4
H α b	b1 6553.83 ± 0.46	154.43 ± 7.35	b1 346 ± 15
	b2 6571.93 ± 0.49		b2 313 ± 20
[N II] λ6583	6584.85 ± 0.06	8.35 ± 0.61	100 ± 7
[S II] λ6718	6717.66 ± 0.14	2.88 ± 0.35	248 ± 29
[S II] λ6732	6732.08 ± 0.18	2.23 ± 0.33	246 ± 0
[Fe XI] λ7892	7891.36 ± 0.22	9.42 ± 0.73	267 ± 21
[Fe XI] off	7899.4 ± 0.08	2.2 ± 0.28	43 ± 8
[S III] λ9071	9070.98 ± 0.35	3.01 ± 0.69	152 ± 32
[S III] λ9533	9532.54 ± 0.09	5.83 ± 0.44	80 ± 7

Table A2. Results from Gaussian fits to emission lines in the Feb 2021 spectrum, after correction to instrumental resolution, which varies from 75 to 150 km s^{-1}. As discussed in the text, we estimate that line fluxes have an addition ∼15 per cent systematic error.

Line	Centre Å	Flux 10^{-16} (erg s^{-1}cm^{-2})	FWHM (km s^{-1})
[O III] λ4959	4956.88 ± 0.04	16.83 ± 0.46	102 ± 5
[O III] λ5007	5004.93 ± 0.02	49.64 ± 0.69	109 ± 3
[Fe XIV] λ5304	5304.02 ± 1.86	4.26 ± 3.73	297 ± 145
[Fe VII] λ6087	6088.21 ± 0.16	5.08 ± 0.49	125 ± 19
[Fe X] λ6375	6374.91 ± 0.19	15.38 ± 1.04	300 ± 27
[N II] λ6549	6550.94 ± 0.31	5.17 ± 0.47	180 ± 2
Hα n	6564.36 ± 0.04	16.13 ± 0.83	<120 ± 5
Hα b	b1 6555.83 ± 0.47	228 ± 10.0	b1 405 ± 15
	b2 6573.58 ± 0.33		b2 255 ± 18
[N II] λ6583	6585.32 ± 0.11	15.52 ± 1.4	179 ± 2
[S II] λ6718	6715.1 ± 0.25	3.11 ± 0.55	73 ± 18
[S II] λ6732	6729.4 ± 0.2	3.81 ± 0.59	73 ± 18
[Fe XI] λ7892	7892.44 ± 0.2	11.39 ± 0.84	240 ± 20

Table A3. Results from Gaussian fits to emission lines in the 2022 January spectrum, after correction for instrumental resolution, which is approximately 56 km s^{-1} for blue arm lines, $\lambda < 5600$ Å, and 34 km s^{-1} for red arm lines, $\lambda > 5600$ Å. As discussed in the text, we estimate that line fluxes have an addition ∼15 per cent systematic error.

Line	Centre (Å)	Flux 10^{-16} (erg s^{-1}cm^{-2})	FWHM (km s^{-1})
[Ne V] λ3426	3426.26 ± 0.06	4.57 ± 0.59	68 ± 13
[O II] λ3727	3729.61 ± 0.08	4.46 ± 0.44	112 ± 10
[O II] λ3729	3726.72 ± 0.08	4.12 ± 0.43	112 ± 10
[Ne III] λ3869	3869.25 ± 0.05	5.65 ± 0.38	116 ± 9
[He II] λ4686	4686.62 ± 0.09	2.82 ± 0.36	118 ± 16
H β	4862.24 ± 0.03	8.61 ± 0.86	90 ± 6
[O III] λ4959	4959.41 ± 0.04	8.21 ± 0.46	70 ± 5
[O III] λ5007	5007.3 ± 0.02	31.8 ± 0.69	86 ± 2
[Fe XIV] λ5304	5303.71 ± 0.29	4.76 ± 0.87	214 ± 38
[Fe VII] λ6087	6087.45 ± 0.31	2.33 ± 0.57	107 ± 37
[O I] λ6300	6301.4 ± 0.09	3.98 ± 0.5	79 ± 11
[Fe X] λ6375	6374.86 ± 0.18	14.14 ± 0.85	328 ± 21
[N II] λ6549	6549.67 ± 0.1	4.03 ± 0.17	94 ± 4
H α n	6564.02 ± 0.01	45.37 ± 0.56	94 ± 1
H α b	b1 6556.15 ± 1.45	85.44 ± 15.04	b1 358 ± 32
	b2 6572.48 ± 2.38		b2 363 ± 60
[N II] λ6583	6584.83 ± 0.03	12.08 ± 0.52	93 ± 4
[S II] λ6718	6717.84 ± 0.12	3.08 ± 0.31	106 ± 10
[S II] λ6732	6732.23 ± 0.14	2.72 ± 0.3	105 ± 10
[O I] λ7321	7321.32 ± 0.18	2.2 ± 0.37	107 ± 19
[Fe XI] λ7892	7892.85 ± 0.11	8.67 ± 0.5	171 ± 11
[S III] λ9071	9070.46 ± 0.12	5.58 ± 0.5	119 ± 10
[S III] λ9533	9532.54 ± 0.05	12.41 ± 0.5	95 ± 4

APPENDIX B: EVOLUTION OF IRON CORONAL LINES

In this section, we plot coronal line regions from 8 epochs of X-Shooter and MUSE spectra. All plots display a wavelength region ranging from −1500 to 1500 km s^{-1} centred on the relevant line. In each case, the flux is normalized to the median value of that region.

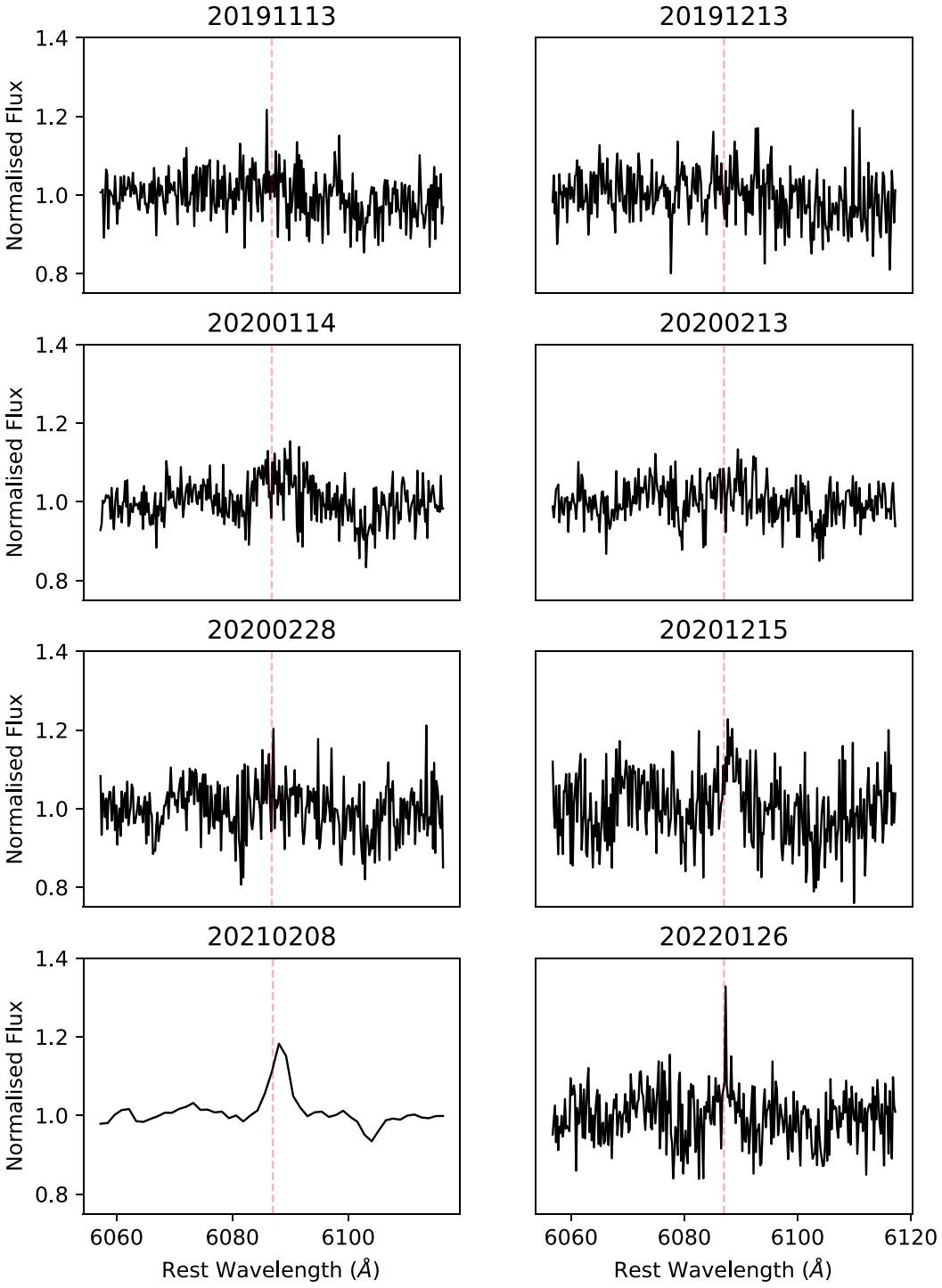

Figure B1. Evolution of the [Fe VII] λ 6087 coronal line region.

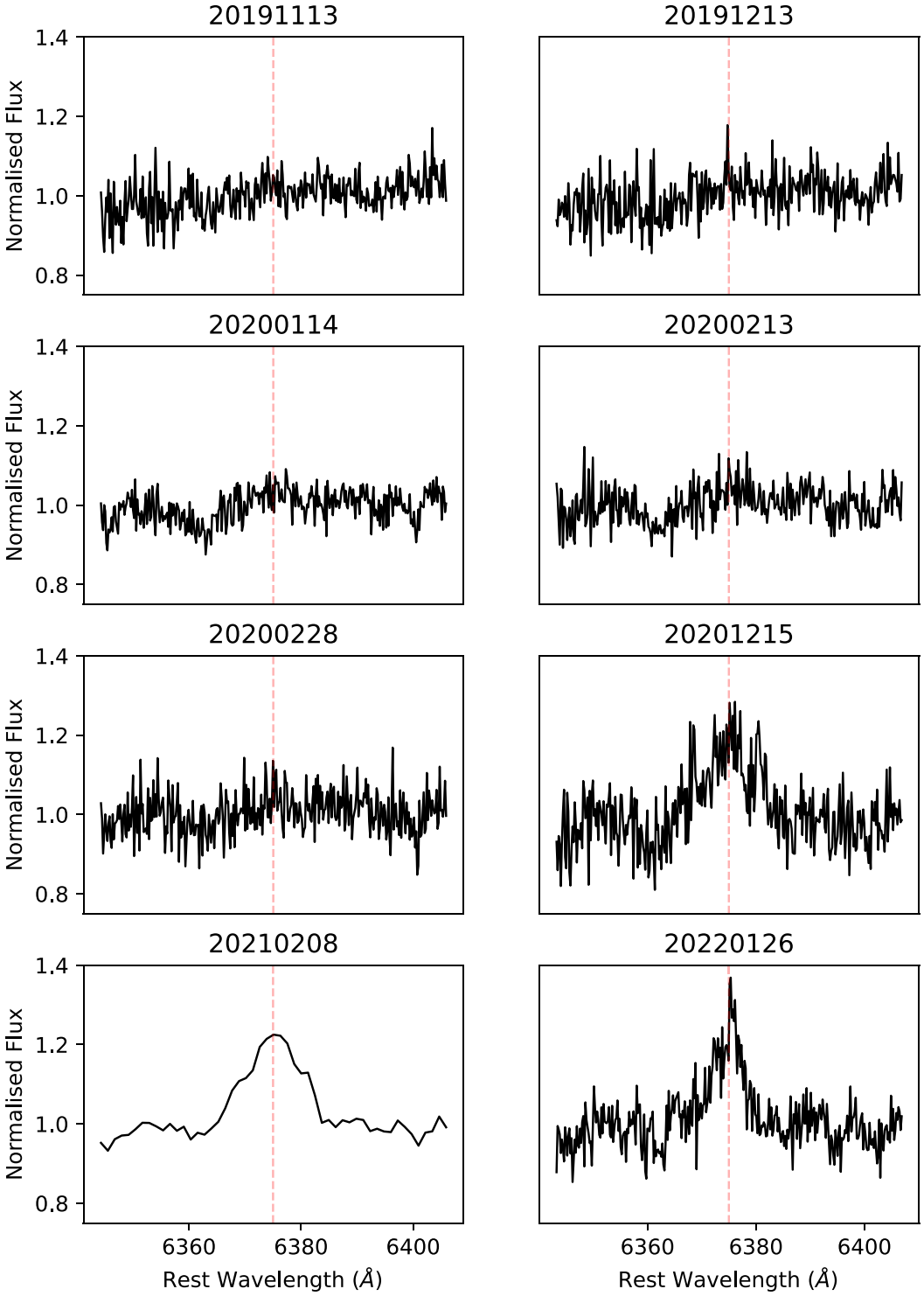

Figure B2. Evolution of the [Fe X] λ 6375 coronal line region.

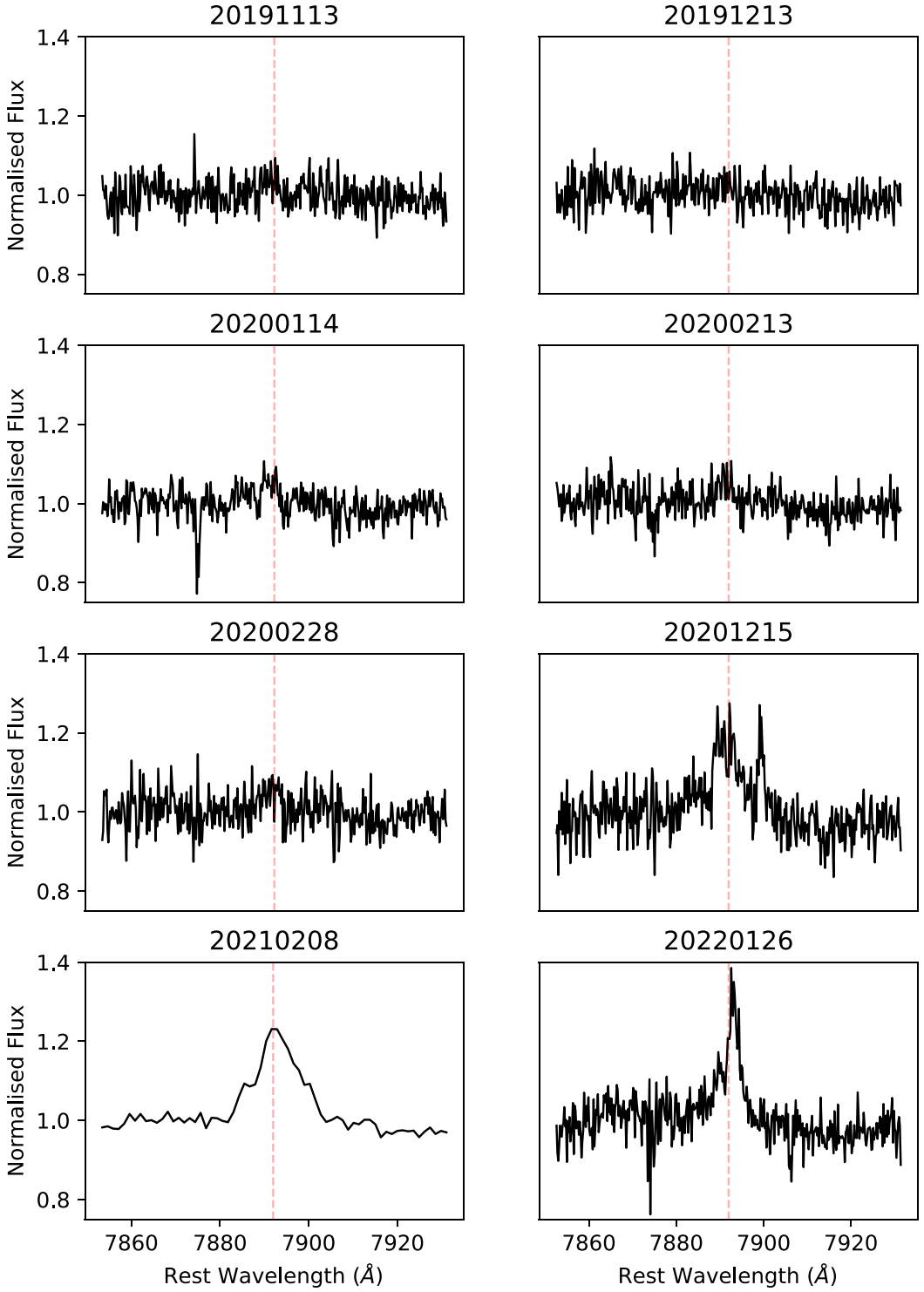

Figure B3. Evolution of the [Fe XI] λ 7892 coronal line region.

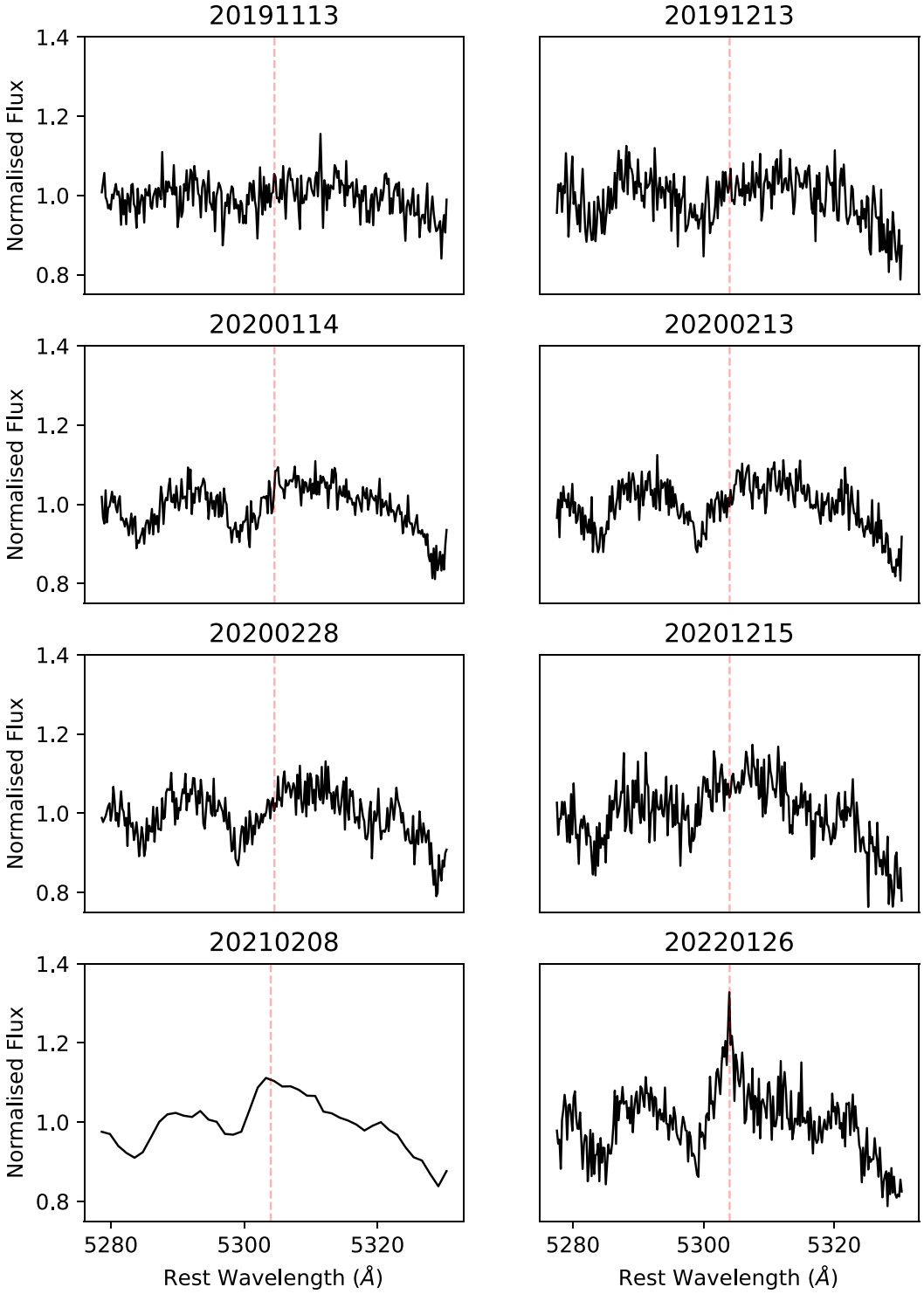

Figure B4. Evolution of the [Fe XIV] λ 5304 coronal line region.

This paper has been typeset from a TEX/LATEX file prepared by the author.